The developmental changes in intrinsic and synaptic properties of prefrontal neurons enhance local network activity from the second to the third postnatal week in mice

Katerina Kalemaki[1,2], Xiaxia Xu[3], Angeliki Velli[2,4], Ourania Christodoulou[4,5], Myrto Denaxa[5] Ileana L. Hanganu-Opatz[3], Domna Karagogeos[1, 2*] and Kyriaki Sidiropoulou[2,4*]

[1]Department of Basic Science, Faculty of Medicine, University of Crete, Heraklion, Greece

[2]Institute of Molecular Biology and Biotechnology (IMBB), FORTH, Heraklion, Greece

[3]Developmental Neurophysiology, Institute of Neuroanatomy, University Medical Center Hamburg-Eppendorf, Hamburg, Germany

[4]Department of Biology, University of Crete, Heraklion, Greece

[5]BSRC 'Alexander Fleming'

[*] co-corresponding author and equal senior contribution

Abstract

The prefrontal cortex (PFC) is characterized by protracted maturation that extends until adulthood. The cellular mechanisms controlling the early development of prefrontal circuits are still largely unknown. Our study delineates the developmental cellular processes that are on-going in the mouse medial PFC (mPFC) during the second and third postnatal weeks and compares them to those in the barrel cortex (BC). We show that from the second to the third postnatal week in both brain areas due to increased spontaneous inhibitory postsynaptic currents (sIPSC) and reduced spontaneous excitatory postsynaptic currents (sEPSC) ones. Drug application suggested that the increased sEPSC frequency at mPFC at P10 is due to depolarizing $GABA_A$ receptor ($GABA_AR$) function. Evoked IPSC recordings revealed that the $GABA_AR$ in mPFC at P10 exhibits significantly depolarizing reversal potential, compared to mPFC at P20. Additionally, the K-Cl co-transporter 2 (KCC2) expression is decreased in the neonatal mPFC compared to the juvenile reinforcing the idea that $GABA_AR$ function in the neonatal mPFC is depolarizing. Furthermore, increasing $GABA_AR$ activity leads to increased basal synaptic response and spontaneous activity of neonatal mPFC, but not BC. Moreover, the GABAergic interneurons in the neonatal mPFC exhibit immature active properties. The above developmental changes in the synaptic and intrinsic properties of mPFC neurons contribute to

32 the enhanced network activity in the juvenile mPFC, compared to neonatal mPFC, using a
33 computational modeling approach, a result that was then confirmed by in vivo recordings.
34
35 **Abbreviations**
36 BC: Barrel Cortex
37 INs: Interneurons
38 KCC2: K-Cl co-transporter 2
39 NKCC1: Na^+-K^+-Cl^- cotransporter 1
40 mPFC: medial Prefrontal Cortex
41 P10: Postnatal day 10
42 P20: Postnatal day 20
43 PNs: Pyramidal neurons
44 sEPSC: spontaneous excitatory postsynaptic current
45 sIPSC: spontaneous inhibitory postsynaptic current
46 YFP: yellow fluorescent protein
47 PV: parvalbumin
48 SST: somatostatin
49
50 **Introduction**
51 During early postnatal development, major events that contribute to cortical circuit
52 maturation include spatial and temporal patterns of electrical activity, intrinsically determined
53 cell death of early postnatal cortical interneurons and the depolarizing action of the
54 neurotransmitter GABA (γ-aminobutyric acid) (Khazipov et al. 2004; Khazipov and Luhmann
55 2006; Allene et al. 2008; Brockmann et al. 2011; Ben-Ari et al. 2012; Southwell et al. 2012;
56 Khazipov et al. 2013; Kirmse et al. 2015; Mòdol et al. 2019). The developmental switch of GABA
57 action from depolarizing to hyperpolarizing results from changes in chloride co-transporter
58 expression: Na^+-K^+-Cl^- cotransporter 1 (NKCC1), the Cl^- importer, is highly expressed early in
59 development, while the expression of the co-transporter KCC2, the Cl^- exporter, increases after
60 the first postnatal week (Ben-Ari 2001; 2002; Ben-Ari et al. 2007; Ben-Ari 2012). In addition, both
61 intrinsic properties of neurons and synaptic transmission undergo dramatic changes during early
62 postnatal development in a brain-area specific manner (Kriegstein et al. 1987; McCormick and
63 Prince 1987; Burgard and Hablitz 1993; Ramoa and McCormick 1994; Bahrey and Moody 2003).

Most studies on these developmental changes of the GABAergic system in the cortex have focused on the primary somatosensory cortex, visual cortex and hippocampus (Bartolini et al. 2013; Le Magueresse and Monyer 2013; Hensch 2016). The barrel cortex (BC) is part of the primary somatosensory cortex and is organized vertically in columns of cells associated with sensory perception (Guo et al. 2014) and horizontally in six layers of distinct cell types. In contrast, cortical association areas such as the prefrontal cortex (PFC) regulate cognitive functions and do not directly control sensory information (Fuster 2015). Anatomically, the mouse medial PFC (mPFC) is defined as the agranular part of frontal lobe, lacking the prominent granular layer IV and is divided into distinct subregions, namely infralimbic, prelimbic and cingulate cortex (Heidbreder and Groenewegen 2003; Van De Werd et al. 2010). The timeline of mPFC development is delayed compared to other sensory cortices, such as BC (Casey et al. 2000; Best and Miller 2010; Kolb et al. 2012, Rinetti-Vargas et al., 2017). From infancy to adulthood, the developing mPFC undergoes considerable transcriptional, structural and functional changes (Diamond 2005; Tsujimoto 2008; Kolb et al. 2012; Schubert et al. 2014; Kroeze et al. 2017).
While adolescent development of prefrontal circuitry and the underlying cellular mechanisms have been addressed by a large number of studies, few investigations tackled the wiring processes at earlier stages (Brockmann et al. 2011; Bitzenhofer et al. 2015; 2017), in particular he mPFC between the second (neonatal) and third (juvenile) postnatal week. Here, we aim to fill this gap by investigating the synaptic and intrinsic properties of neonatal and juvenile mPFC neurons and comparing them to those in the BC, with a primary focus on the GABAergic system.

Methods

All *in vitro* experiments with mice took place under an experimental protocol approved by the Research Ethics Committee and by our Institutional Animal Care and Use Committee that has been approved by the Veterinarian Authorities Office (protocol license no. 93164). Experiments were carried out by trained scientists and in accordance with the 3R principles. *In vivo* experiments were performed in compliance with the German laws and the guidelines of the European Community for the use of animals in research and were approved by the local ethical committee (015/17, 015/18).

Animals

95 The *in vitro* experiments were performed on male C57Bl/6J; Lhx6Tg(Cre); R26R-YFP+/+ mice
96 from animal facility of IMBB-FORTH were used. For the *in vivo* experiments, timed-pregnant
97 C57BL/6J mice from the animal facility of the University Medical Center Hamburg-Eppendorf
98 were used. The day of vaginal plug detection was defined as embryonic day (E)0.5, whereas the
99 day of birth was defined as P0. The offspring of both sexes are used for *in vivo* electrophysiology
100 recordings. All procedures were performed according to the European Union ethical standards
101 outlined in the Council Directive 2010/63EU of the European Parliament on the protection of
102 animals used for scientific purposes.
103 Mice were housed with their mothers and provided with standard mouse chow and water ad
104 libitum, under a 12 h light/dark cycle (light on at 7:00 am) with controlled temperature (21°C).
105 The P10 experimental group includes ages P9-P11 and the P20 group includes ages P19-P21, also
106 referred to as second and third postnatal weeks or neonatal and juvenile, respectively. All efforts
107 were made to minimize both the suffering and the number of animals used.
108
109 ***In vitro* extracellular recordings**
110 Slice Preparation*:* Mice (P10 and P20) were decapitated under halothane anesthesia. The brain
111 was removed promptly and placed in ice cold, oxygenated (95% O_2 –5% CO_2) artificial
112 cerebrospinal fluid (aCSF) containing (in mM): 125 NaCl, 3.5 KCl, 26 $NaHCO_3$, 1 $MgCl_2$ and 10
113 glucose (pH = 7.4, 315 mOsm/l). The brain was blocked and glued onto the stage of a vibratome
114 (Leica, VT1000S). Rostrocaudal coronal slices (400 µm thick) containing either the mPFC
115 (prefrontal cortex) or the BC (barrel cortex) region were selected and transferred to a submerged
116 chamber, which was continuously superfused with oxygenated (95% O_2 –5% CO_2) aCSF
117 containing (in mM): 125 NaCl, 3.5 KCl, 26 $NaHCO_3$, 2 $CaCl_2$, 1 $MgCl_2$ and 10 glucose (pH = 7.4, 315
118 mOsm/l) at room temperature (RT). The slices were allowed to equilibrate for at least 1 h in this
119 chamber before recordings began. Slices were then transferred to a submerged recording
120 chamber, continuously superfused with oxygenated (95% O_2 –5% CO_2) aCSF (same constitution
121 as the one used for maintenance of brain slices) at RT during recordings.
122 Data Acquisition: Electrophysiological recordings were performed in all experimental groups
123 under the same conditions as described below. Pulled glass micropipettes were filled with NaCl
124 (2M) and placed in layers II/III of PFC and BC. Platinum/iridium metal microelectrodes (Harvard
125 apparatus United Kingdom, 161 Cambridge, United Kingdom) were placed on layer II/III of the
126 mPFC and the BC, about 300 µm away from the 1MΩ recording electrode, and were used to

evoke field excitatory postsynaptic potentials (fEPSPs). Local field potentials (LFPs) were amplified using a headstage with selectable high pass filter of 30 Hz to remove any offsets coupled to a Dagan BVC-700A amplifier, amplified 100 times and low-pass filtered at 1-kHz. A notch filter was used to eliminate line frequency noise at 30 Hz. Signals were digitized using the ITC-18 board (InstruTech, Inc.) on a PC with custom-made procedures in IgorPro (Wavemetrics, Inc.) and stored on a PC hard drive. All voltage signals were collected at a sampling frequency of 100 kHz (fs = 100 kHz).

For evoked fEPSPs, the electrical stimulus consisted of a single square waveform of 100 μs duration given at intensities of 0.1– 0.3 mA (current was increased from 0.1 mA to 0.3 mA, with 0.1 mA steps) generated by a stimulator equipped with a stimulus isolation unit (World Precision Instruments, Inc.). The effect of $GABA_AR$ activation was investigated by bath application of 2 μM Diazepam ($GABA_AR$ agonist). Diazepam was acquired from the Pharmacy of the University General Hospital in Heraklion as a 5 mg/ml solution and was diluted in aCSF during recordings. Other drugs used include CNQX (10μM), AP5 (50μM) and bumetanide (10μM) (Tocris). For spontaneous activity recordings, 20 5-sec recordings were acquired without any stimulation.

Data Analysis: Data were analyzed using custom-written procedures in IgorPro software (Wavemetrics, Inc.). No additional high-pass filters were applied to the raw data. For evoked recordings, the peak values of the fEPSP were measured using the minimum value of the synaptic response (4–5 ms following stimulation) and were compared to the baseline value prior to stimulation. Both parameters were monitored in real- time in every experiment. A stimulus–response curve was then plotted using stimulation intensities between 0.1 and 0.8 mA, in 0.1 mA steps. For each different intensity level, two traces were acquired and averaged.

To identify spontaneous activity events, the acquired spontaneous activity voltage signals of 5 seconds' duration were decimated (down-sampled) by a factor of 10 and the standard deviation σ_b of background signal was calculated in the 'quiet' part of each voltage response trace. To identify the 'quiet' period, each 5sec trace was split into 100msec increments and the range of voltage deflection was computed in each increment. The 'quiet' part of the LFP trace was the 100msec increment with the smallest σ_b value. As a spontaneous event, any voltage response larger than $4 \cdot \sigma_b$ was identified. We calculated the frequency of spontaneous events by measuring the number of spontaneous events divided by the duration of the trace (5s). The frequency was calculated in 20 consecutive 5-sec traces and then averaged for each condition

158 animal. The spontaneous events do not correspond to spiking of individual neurons, they rather
159 reflect population spikes.
160
161 ***In vitro* patch-clamp recordings**
162 Slice Preparation: Mice were decapitated under halothane anesthesia. The brain was removed
163 immediately and coronal slices of mPFC and BC (300–350 µm thick), using a vibratome (Leica,
164 VT1000S, Leica Biosystems) were prepared from mice at the ages of P10 and P20 in ice-cold
165 oxygenated (95% O_2 - 5% CO_2) modified choline-based aCSF (in mM) 0.5 $CaCl_2$, 7 mM $MgSO_4$;
166 NaCl replaced by an equimolar concentration of choline). Slices were incubated for 30min at
167 32°C in an oxygenated normal aCSF containing (in mM): 126 NaCl, 3.5 KCl, 1.2 NaH_2PO_4, 26
168 $NaHCO_3$, 1.3 $MgCl_2$, 2.0 $CaCl_2$, and 10 D-glucose, pH 7.4, 315 mOsm/l. Slices were allowed to
169 equilibrate for at least 30 min at RT before being transferred to the recording chamber. During
170 recordings, slices were perfused at a rate of 4 ml/min with continuously aerated (95% O_2-5%
171 CO_2) normal aCSF at RT.
172 Data Acquisition: Neurons were impaled with patch pipettes (5–7 MΩ) and recorded in the
173 whole-cell configuration, either in the current-clamp or voltage-clamp mode. For current-clamp
174 experiments, the composition of the intracellular solution was: 130 mM K-$MeSO_4$, 5 mM KCl, 5
175 mM NaCl, 10 mM HEPES, 2.5 mM Mg-ATP, and 0.3 mM GTP, 265–275 mOsm, pH 7.3. For voltage-
176 clamp experiments, the composition of the intracellular solution was: 120 mM Cs-gluconate,
177 20mM CsCl, 0.1 mM $CaCl_2$, 1 mM EGTA, 0.4 mM Na-guanosine triphosphate, 2mM Mg-adenosine
178 triphosphate, 10 mM HEPES. No correction from liquid junction potential was applied between
179 the pipette and the aCSF. Whole-cell measurements were low-pass filtered at 5 kHz using an
180 Axopatch 200B amplifier (Molecular Devices, Inc). Recordings were digitized with the ITC-18
181 board (Instrutech, Inc) on a PC using custom-made codes in IgorPro (Wavemetrics, Inc). All
182 signals were collected at a sampling frequency of 20kHz.
183 Data Analysis: Data were analyzed using custom-written codes in IgorPro software
184 (Wavemetrics, Inc.). For passive membrane properties, the resting membrane potential (RMP,
185 mV) was measured within 3 min after establishing the whole-cell configuration, and monitored
186 throughout the experiment. To measure input resistance, a 500ms step-pulse protocol was used
187 with current stimulation from -200pA to +50pA. The input resistance (R_{in}, MΩ) was measured by
188 plotting the steady-state voltage deflection in an I-V plot and calculating the slope of the best fit
189 line curve (R_{in}=V/I). The τ_m (membrane time constant, ms) was obtained by fitting a single

190 exponential curve to the voltage deflection at -50pA, and the membrane capacitance (C_m) was
191 calculated using the formula $C_m = \tau_m/R_{in}$. In addition, the number of spikes generated in response
192 to a 500ms step-pulse range from +100pA to +300pA was measured.
193 To measure action potentials (APs) properties, we applied small supra-threshold 5ms step-pulse
194 currents to the cell from -65mV. The active properties were measured at the minimum current
195 stimulation (Rheobase, pA) that generated an AP. The AP threshold (mV) was calculated by
196 taking the first derivative of the voltage trace, defining a threshold and identifying the voltage
197 level at that time point. The rate of rise of the AP (dV/dt, mV/ms) was the maximum value of
198 that first derivative trace. The AP amplitude (mV) was defined as the voltage difference between
199 AP threshold and AP peak. The AP duration (ms) was calculated by the full width of the waveform
200 at the half maximal amplitude (half-width). The fast afterhyperpolarization (fAHP) minimum
201 (mV) was defined as the minimum voltage right after the AP. The fAHP amplitude (mV) was
202 calculated as the difference between the AHP minimum and the AP threshold. The fAHP time
203 (ms) was defined as the time duration from the time point of AP threshold to the fAHP minimum.
204 Voltage-clamp/spontaneous IPSC and EPSCs
205 The composition of our intracellular solution resulted in chloride reversal potential of -60mV and
206 Na^+/K^+ reversal potential of +10mV. This allowed for measurements of spontaneous excitatory
207 postsynaptic currents (sEPSCs) to be recorded at -60mV and of spontaneous inhibitory
208 postsynaptic currents (sIPSCs) to be recorded at +10mV. Automatically selected events were
209 subsequently visually monitored to discard erroneously included noise. The events showing only
210 single peaks were selected for kinetics analysis. All currents detected from every single neuron
211 were averaged. The peak amplitude was calculated as the maximum current value. The time
212 constant of the decay phase was detected by curve fitting with a single exponential decay
213 function.
214 Evoked IPSC recordings: To investigate eIPSCs and the reversal potential, a stimulating electrode
215 was positioned 100µm away from the recording electrode at the border between layer I and
216 layer II. The current used for stimulation was adjusted to give a 100-300pA response at -70mV.
217 For p10 recordings, the current used was 0.3mA while for p20 recordings the current used was
218 0.1mA. Recordings were taken at different voltage steps, from -80mV to +40mV in the presence
219 of CNQX (20µM) and AP5 (50µM).
220
221 ***In vivo* extracellular recordings**

222 Surgery: Multisite extracellular recordings were performed in the PFC of P8–P10 (n=13) and P20–
223 P23 (n=14) C57/BL mice with both sexes. Mice were under urethane anesthesia (intraperitoneal
224 injection, 1 mg/g body weight; Sigma-Aldrich) before surgery. The bone over the mPFC (0.8 mm
225 anterior to bregma, 0.1–0.5 mm right to the midline) was carefully removed. One-shank
226 electrodes with 4 recording sites (0.4–0.8 MΩ impedance, 100 µm spacing, NeuroNexus) was
227 inserted into PFC at a depth of 1.9 mm from the skull surface. Electrodes were labelled with DiI
228 (1,1'-dioctadecyl-3,3,3',3'-tetramethyl indocarbocyanine; Invitrogen) to confirm their position
229 after histological assessment post-mortem. One silver wire was inserted into the cerebellum to
230 serve as ground and reference electrode.
231 Data Acquisition: A recovery period of 10 min following the insertion of electrodes before
232 acquisition of data was provided. Data acquired during the first 30 min of recording were used
233 for analysis to ensure similar state of anesthesia in all investigated pups. Extracellular signals
234 were bandpass filtered (0.1 Hz to 5 kHz) and digitized (32 kHz) with a multichannel extracellular
235 amplifier (Digital Lynx SX, Neuralynx) and the Cheetah acquisition software (Neuralynx).
236 Data Analysis: Data were imported and analyzed off-line using custom-written tools in MATLAB
237 software version 7.7 (MathWorks). Multiple unit activity (MUA) is detected when negative
238 deflections exceeding five times the SD of the bandpass filtered (500–5000 Hz) signals. Single
239 unit activity (USA)- was detected and clustered using klusta (Rossant et al., 2016) and manually
240 curated using phy (https://github.com/cortex-lab/phy). Data were imported and analyzed using
241 custom-written tools in the MATLAB. Burst activity was detected by using the method from
242 (Gorin, Tsitoura et al. 2016). First, for each unit, Poisson distribution, which assumed random
243 independent spiking, was defined. The single parameter λ of Poisson distribution is the average
244 firing rate of the unit. Second, the median interspike interval (ISI) value of the Poisson
245 distribution was derived. Third, we defined a burst activity as a sequence of ≥4 consecutive
246 spikes separated by intervals smaller than the median ISI. Last, the percentage of the burst
247 activity of a single unit is calculated by 100* (the number of the burst activity / the number of
248 the spikes). A unit was classified as "burst unit" if >50% of all spikes occurred in bursts.
249
250 **Immunohistochemistry**
251 Mice at the age of P10 and P20 were perfused with 4% paraformaldehyde, followed by fixation
252 with the same solution for 1h at 4◦C, followed by cryoprotection and preparation of 12 µm
253 cryostat sections as previously described[88]. Primary antibodies used were rat monoclonal anti-

254 GFP (Nacalai Tesque, Kyoto, Japan, 1:5000), rabbit polyclonal anti-GFP (1:500; Minotech
255 Biotechnology, Heraklion, Greece) and rabbit polyclonal anti-
256 parvalbumin (PV) (Swant, Bellinzona, Switzerland; 1:2000. Secondary antibodies used were goat
257 anti-rat-Alexa Fluor-488, goat anti-rabbit Alexa Fluor-488, and goat anti-rabbit-Alexa Fluor-555
258 (Molecular Probes, Eugene, OR, United States, 1:800). Images were obtained with a confocal
259 microscope (Leica TCS SP2, Leica, Nussloch, Germany). For each age group (P10, P20), 2-4 10µm-
260 thick sections from each mouse brain were selected, all including the mPFC and BC.
261
262 **RNA *In Situ* Hybridization**
263 Non-radioactive *in situ* hybridization experiments were performed on cryostat sections (12µm
264 thick, see immunochemistry) according to the protocol described (Schaeren-Wiemers and
265 Gerfin-Moser 1993). Riboprobe was prepared by *in vitro* transcription and was specific
266 Somatostatin (SST) (Liodis et al. 2007).
267
268 **Nissl Staining**
269 Cryostat sections (12µm thick, see immunochemistry) were incubated in 1:1 100%
270 ethanol:chloroform overnight at RT. Then, sections were rehydrated for 1 min in 100%, 95%
271 ethanol solutions and dH_2O at RT, followed by a 10-min incubation in 0.1% cresyl violet solution
272 at 50°C. Sections were then dehydrated with dH_2O, 95%, 100% ethanol and xylene for 5 min and
273 coverslipped with permount. Images from whole sections were obtained in 5× magnification of
274 a light microscope (Axioskop 2FS, Carl Zeiss AG, 268 Oberkochen, Germany) and merged using
275 Adobe Photoshop CC 2015, Adobe Systems, Inc.
276
277 **Analysis for Immunochemistry, *in situ* hybridization and Nissl staining**
278 Images taken from Nissl staining slices were analyzed with Matlab, using a custom-made
279 algorithm, which was double checked with hand-counting (Konstantoudaki et al. 2016;
280 Chalkiadaki et, 2019). Images from immunochemistry and in situ hybridization experiments,
281 were hand counted using ImageJ.
282
283 **Western blots**
284 Mice were decapitated following cervical dislocation, the brain was quickly removed, placed in
285 ice cold PBS (phosphate-buffered saline) and then positioned on a brain mould, where 1.5 mm

286 slices were taken containing the mPFC and BC. The slices were placed on dry ice, and the
287 prelimbic area of mPFC was dissected out and stored at -80ºC. The BC was also isolated from the
288 corresponding slices and stored at -80ºC. Frozen tissue blocks were lysed in a solution containing
289 (in mM) HEPES 50, NaCl 150, MgCl2 1.5, EGTA 5, Glycerol 1%, Triton-X100 1%, 1:1000 protease
290 inhibitors cocktail. Proteins ran on 8.5% bis-acrylamide gel and were transferred onto a
291 nitrocellulose membrane (Whatman GmbH, Dassel, Germany). The membrane was blocked,
292 incubated in rabbit polyclonal anti-K+/Cl-Cotransporter (KCC2) (Merck KGaA, Darmstadt,
293 Germany, 1:1000) or rabbit monoclonal anti-GAPDH (Cell Signaling Technology Europe BV,
294 Leiden, Netherlands, 1:1000), washed, incubated in secondary goat anti-rabbit IgG Horseradish
295 Peroxidase Conjugate antibody (Invitrogen, 1:5000), and digitally exposed using the Molecular
296 Imaging system ChemiDoc (BioRad Laboratories, Inc, California, U.S.A.). Analysis of KCC2 and
297 GAPDH expression was performed with ImageJ software, and the raw values of KCC2 from each
298 sample were normalized to their respective GAPDH values.
299
300 **Statistical analysis**
301 Statistical analyses were performed in Microsoft Office Excel 2007 and GraphPad Prism Software
302 7.0. Data are presented as mean ± standard error of mean (SEM). Normality distribution and
303 equality of variances of dataset were tested with the Kolmogorov-Smirnov test normality test.
304 The null hypothesis was rejected for a >5%. When four experimental groups (P10 mPFC, P20
305 mPFC, P10 BC and P20 BC) were assessed and two variables were taken into consideration (age
306 and brain area), data were analyzed with a two-way ANOVA with Fisher LSD, Sidak's or Tukey's
307 multiple comparisons (electrophysiological recordings and cell counting). When three groups
308 (P10 mPFC, P20 mPFC and P10 BC) data were analyzed with one-way ANOVA
309 (electrophysiological recordings). For the comparison of *in vivo* spiking activity between P10 and
310 P20, statistical analyses were performed with MATLAB. Significant differences were detected by
311 one-way ANOVA. Significance levels of *$p < 0.05$, **$p < 0.01$, ***$p < 0.001$ or ****$p < 0.0001$
312 were tested. For comparison of Western blot analysis, the significant effect of each
313 developmental age group from mPFC and BC was assessed using Student's t-test depending on
314 the experiment.
315
316 **Modeling**

317 We adapted the PFC microcircuit model we had developed previously (Konstantoudaki et al.,
318 2014) to fit our experimental data with regards to intrinsic properties of pyramidal neurons and
319 fast-spiking interneurons. We generated two model networks: a) a neonatal mPFC model
320 network and b) a juvenile mPFC model network. In the neonatal mPFC model network the
321 following adjustments were made: a) the pyramidal model neuron was adjusted to fit the passive
322 and active properties of the neurons recorded in this paper, primarily the neonatal pyramidal
323 model neuron exhibited increased input resistance and reduced spike amplitude, b) the fast-
324 spiking interneuron model neuron was adjusted to have reduced fast afterhyperpolarization, as
325 found in our experiments and c) the $GABA_AR$ receptor model had a reversal potential of -40mV.
326 In the juvenile mPFC model network, the following adjustments were made: a) the $GABA_AR$
327 receptor model had a reversal potential of -60mV. All other properties were maintained as in
328 the original model. The network was stimulated with spontaneous synaptic activation on
329 pyramidal model neurons with characteristics similar to the sEPSC and sIPSC properties we
330 recorded. Each condition was simulated in 10 different trials. In each trial, the location of
331 activated synapses varied.
332
333 **Data availability**
334 Data presented in the figures in this paper are available upon request.
335
336 **Results**
337 Mice belonging to two age groups were investigated: (i) neonatal mice included pups of
338 postnatal days (P) 9-11 and are defined as P10 while (ii) juvenile mice defined as P20 animals
339 included pups of P19-P21. Due to the high density of intra-cortical synapses in the superficial
340 cortical layers (DeFelipe and Fariñas 1992; Clancy et al. 2001) and their specific involvement in
341 neurodevelopmental disorders (Chini and Hanganu-Opatz, 2020; Bitzenhofer eta l., 2017) we
342 focused on the superficial layers of the mPFC and BC. From each mouse brain, both the mPFC
343 and the BC were studied. All analyses that had four groups (mPFC P10 and P20, BC P10 and P20)
344 were conducted using two-way ANOVA, with the two factors being the brain area (mPFC and
345 BC) and age (P10 and P20).
346
347 **Synaptic transmission adaptations in mPFC and BC across development**

348 To examine spontaneous synaptic transmission, we performed patch-clamp recordings from
349 layer II/III pyramidal neurons in mPFC and BC from P10 and P20 mice. We recorded spontaneous
350 inhibitory postsynaptic currents (sIPSCs, at +10mV) and spontaneous excitatory postsynaptic
351 currents (sEPSCs, at -60mV) and we measured the frequency, amplitude and decay time
352 constant.
353 In mPFC, the frequency of sIPSCs was significantly augmented at P20 compared to P10 (**Figure**
354 **1a,b**), while the sIPSC amplitude and decay-time constant did not significantly change over the
355 investigated time window (**Figure 1a,c,d**). Similarly, the sIPSC frequency and amplitude were
356 significantly increased, at P20 compared to P10, in BC (**Figure 1a,b,c**), while the decay-time
357 constant was not altered (**Figure 1a,d**). On a different note, the sIPSC in BC at P20 was
358 significantly increased compared to P10 in BC but also compared to P20 in mPFC.
359 The sEPSC frequency was significantly decreased at P20 compared to P10, in both areas (**Figure**
360 **1e,f**), while the amplitude and decay time constant were unaltered (**Figure 1g,h**). Upon
361 comparing the two brain areas, the sEPSC frequency and amplitude were found significantly
362 decreased in mPFC, compared to BC, at P10 (**Figure 1f**). At P20, the sEPSC frequency was similar
363 between the two cortical areas, while the amplitude remained significantly smaller in mPFC
364 compared to BC in both ages (**Figure 1g**). The decay time constant was not different between
365 areas at both ages (**Figure 1h**).
366 We further investigated the changes in sIPSC and sEPSC frequency changes in the mPFC, in
367 particular, in the presence of AMPA and NMDA receptor antagonists, CNQX and AP5, respectively
368 and a $GABA_A$ receptor antagonist, bicuculine. The sIPSC frequency remained increased at P20,
369 compared to P10, CNQX and AP5 (**Figure 2a,c**). On the other hand, bicuculine blocked the sIPSCs
370 both in P10 and P20 mPFC (**Figure 2 b, c**). Application of CNQX eliminated the sEPSCs in mPFC
371 slices at P20 and significantly reduced, but did not eliminate sEPSCs, in mPFC slices at P10 (**Figure**
372 **2e,g**). Application of bicuculine (10uM) did not affect the sEPSC frequency in mPFC slices at P20
373 but significantly reduced sEPSC frequency at mPFC P10 (**Figure 2f,g**). These results suggest that
374 depolarizing $GABA_AR$ currents could contribute to the increased sEPSC frequency observed in
375 layer II/III mPFC pyramidal neurons at P10.
376
377 **GABA is depolarizing in the neonatal mPFC but not BC**
378 Our data so far suggests that $GABA_AR$ function is still depolarizing at P10 in the mPFC. To further
379 investigate this, we performed evoked IPSCs (eIPSCs) at P10 and P20 mPFC in the presence of

380 CNQX and AP5 at different voltage steps. A line curve was fit across the eIPSC currents recorded
381 from -60mV to +10mV, because there was a linear V-I relationship at this range. From the graphs,
382 it is evident that reversal potential at P10 is more positive than -30mV, while the reversal
383 potential at P20 is around -45mV (**Figure 3a,b**).
384 We further investigated the $GABA_AR$ activity by isolating a $GABA_AR$ response in fEPSP recordings
385 by using CNQX and AP5. The addition of diazepam (2µM) (a $GABA_AR$ agonist) increased the fEPSP
386 amplitude in mPFC at P10, but not at P20 (**Figure 4a-b**). In BC, there was no effect of diazepam,
387 either at P10 or P20 (**Supplemental Figure 1**). The switch in the $GABA_AR$ function from
388 depolarizing to hyperpolarizing occurs due to the increased expression of the K^+-Cl^- co-
389 transporter 2 (KCC2) (Rivera et al. 1999). To determine whether modulating chloride
390 transporters could alter the diazepam-induced enhancement of the fEPSP at P10 mPFC, we
391 recorded the fEPSP in the presence of bumetanide (10uM), which blocks the NKCC1 transporter,
392 and tested the effect of diazepam. We find that in the presence of bumetanide, diazepam did
393 not result in an increase of the fEPSP (**Figure 4c-d**). In addition, we measured KCC2 protein levels
394 and demonstrated that they were significantly increased at P20 compared to P10 in the mPFC
395 but not in the BC (**Figure 4e-g**). The above results collectively suggest that the $GABA_AR$ function
396 is depolarizing in the mPFC at P10.
397
398 **Passive and active membrane properties of MGE-derived interneurons are altered in the mPFC**
399 **across development**
400 To investigate whether the change in $GABA_AR$ function in mPFC is also associated with changes
401 in interneuron properties, we performed current-clamp recordings from layer II/III mPFC and BC
402 of $Lhx6^+$ interneurons. For this reason, Lhx6-cre;ROSA26fl-STOP-fl-YFP mice were used in which
403 $Lhx6^+$ interneurons express YFP. Lhx6 is expressed by all post-mitotic and mature MGE-derived
404 interneurons (Liodis et al. 2007), therefore, YFP is expressed in MGE-derived interneurons, which
405 include interneurons that express parvalbumin (PV^+) and somatostatin (SST^+).
406 Upon analysis of the passive properties, we found a significant increase in the input resistance
407 and membrane time constant, as well as a significant decrease in the membrane capacitance in
408 the mPFC at P10 compared to P20 (**Figure 5**). In addition, the input resistance and the membrane
409 time constant were higher at P10 mPFC, compared to BC (P10 and P20). There was no difference
410 in the resting membrane potential (RMP) between ages and brain areas (**Figure 5,**
411 **Supplementary Table 1**).

412 Regarding the active properties, there was no significant difference between ages and brain
413 areas in the AP amplitude, AP threshold and rheobase, fAHP time (duration) (**Figure 5a, d, e, g;**
414 **Supplementary Table 1**). The AP rate of rise (dv/dt) was significantly increased while the AP
415 duration (half-width) was significantly reduced at P20 compared to P10 in both the mPFC and
416 BC (**Figure 6b,c, Supplementary Table 1**). In addition, the fAHP amplitude was significantly lower
417 in the mPFC (**Figure 6f, Supplementary Table 1**), compared to BC. The increased rate of rise and
418 the decreased AP duration are possibly linked with the up-regulation of voltage-dependent
419 sodium channels during development (Huguenard et al. 1988), and in combination with the
420 reduced fAHP amplitude suggest that the mPFC MGE-interneurons at P10 are still quite
421 immature, when compared to adult PV^+/SST^+ interneurons in mPFC (Yang et al. 2013; Pan et al.
422 2017).
423 Overall, these data indicate that some intrinsic properties of interneurons in mPFC change with
424 age (from P10 to P20), reaching values that closer resemble adult MGE-derived interneurons
425 (Yang et al. 2013; Pan et al. 2017). The increased sIPSC frequency of mPFC pyramidal neurons
426 observed at P20, compared to P10 could partly be explained by these altered properties of
427 presynaptic interneurons.
428
429 **Decreased PV interneurons in mPFC compared to BC**
430 An additional explanation for the adaptations in inhibitory transmission could come from
431 alterations in interneuron cell densities. To test this, we quantified the number of interneurons
432 per area in cryosections at P10 and P20 mPFC and BC coronal brain slices of $Lhx6^+$-expressing
433 mice. The YFP^+ positive cells per area (i.e. $Lhx6^+$ cell density) in mPFC and BC was similar between
434 ages, but was significantly lower in the mPFC, compared to BC (**Figure 7a**). But we found no
435 contribution of cell death in the mPFC interneuron population, as the percentage of cell death
436 in $Lhx6^+$ neurons is very low in both P10 mPFC and BC (**Supplementary Figure 2**).
437 The transcription factor Lhx6 is required for the specification and maintenance of main MGE-
438 derived interneurons, PV and SST-positive interneuron subtypes, at postnatal ages (Liodis et al.
439 2007). The neuropeptide SST (both mRNA and protein) is progressively expressed from
440 embryonic to postnatal levels (Bendotti et al. 1990; Forloni et al. 1990). We found that the SST
441 mRNA levels were similar between areas and ages (**Figure 7b**). On the other hand, the
442 emergence of PV immunoreactivity in the mouse cortex shows a delayed development, starting
443 from early postnatal period to adult, with marked area-specific differences(Del Rio et al. 1992).

444 We found that PV was only immunoreactive in BC, and not in mPFC, at P10 (**Figure 7c and**
445 **Supplementary Figure 3**). At P20, PV was immunoreactive in both mPFC and BC, but PV^+ cell
446 density was significantly lower in the mPFC, compared to BC (**Figure 7c**).
447 We also counted the total cell density of mPFC and BC from neonatal and juvenile mice
448 (**Supplementary Figure 4a**) using Nissl staining. In the mPFC, the cell density significantly
449 decreased at P20 compared to P10 (**Supplementary Figure 4b**). On the contrary, in BC, the total
450 cell density significantly increased at P20 compared to P10 (**Supplementary Figure 4b**). When
451 the two brain areas were compared, no difference was found at P10, while the mPFC cell density
452 was significantly lower compared to BC at P20 (**Supplementary Figure 4b**).
453 We further examined whether the alterations in total cell density are derived from alterations
454 in cell density of interneurons by measuring the $Lhx6^+$ neurons over the Nissl-positive cells. No
455 differences were detected between areas and ages (**Supplementary Figure 4c).** These results
456 suggest that the changes in total cell density in mPFC and BC respectively are probably due to
457 changes in other neuronal or glial populations.
458
459 **No significant changes in pyramidal neuron excitability**
460 To determine whether the reduced sEPSC frequency can be explained by changes in pyramidal
461 neuron excitability, we investigated their intrinsic properties. The passive and active properties
462 of these neurons were measured using current-clamp recordings from layer II/III mPFC and BC
463 pyramidal neurons. With regards to passive properties, no significant differences were observed
464 in the RMP, the input resistance and the membrane time constant between brain regions and
465 ages (**Supplementary Figure 5, Supplementary Table 1**). Only the membrane capacitance was
466 significantly increased at P20 compared to P10 (**Supplementary Figure 5d, Supplementary Table**
467 **1**), in both brain areas. In addition, the number of spikes generated with increasing current
468 stimulation was not significantly different between ages and regions (**Supplementary Figure 6**).
469 In terms of active properties, the AP amplitude and rate of rise were increased at P20 compared
470 to P10 mPFC, while the AP half-width, rheobase and threshold were not significantly different
471 (**Figure 8, Supplementary Table 1**). The AP amplitude was also significantly increased at P20,
472 compared to P10 in BC, while the other properties did not change (**Figure 8, Supplementary**
473 **Table 1**). Comparing the two regions at the two ages, we found no significant differences of AP
474 properties of pyramidal neurons (**Figure 8, Supplementary Table 1**). The developmental increase
475 of AP amplitude and rate of rise in the mPFC could be due to the on-going maturation of sodium

476 channels in pyramidal neurons. However, these changes could not account for the reduced
477 sEPSCs in the neonatal, compared to juvenile, mPFC and BC.
478
479 **Effects of mPFC changes in intrinsic and synaptic properties on PFC network activity**
480 In an effort to understand the circuit effects of the aforementioned differences in intrinsic and
481 synaptic properties between p10 and P20 mPFC, we adapted an already validated PFC network
482 model (Konstantoudaki et al., 2014) to our current data to generate a neonatal (P10) mPFC
483 model network and juvenile (P20) mPFC model network. Both model networks were stimulated
484 with spontaneous excitatory and inhibitory inputs based on our results for sEPSC and sIPSC
485 frequency at P10 and P20 (**Figure 1 and Supplementary Table 1**). Our simulation results predict
486 that the intrinsic and synaptic changes from P10 to P20 in mPFC result in enhanced mPFC
487 network activity at P20, compared to P10 (**Figure 9a,e**), as indicated by single-cell activity (**Figure**
488 **9a,b**) and the filtered signal (**Figure 9c,d**). Furthermore, we investigated which adaptations have
489 a significant contribution to the network activity properties observed in each model network.
490 Therefore, we generated neonatal model networks in which the pyramidal model neuron used
491 had P20 properties (N2 network), the fast-spiking interneuron model used had P20 properties
492 (N3 network) and the $GABA_AR$ reversal potential was that of P20 (N4 network). We identify that
493 in all the above networks, the resulting neuronal activity generated was significantly reduced
494 compared to the control P10 network (N1) (**Figure 9f**). Similarly, we generated juvenile model
495 networks in which the pyramidal model neuron used had P10 properties (J2 network), the fast-
496 spiking interneuron model used had P10 properties (J3 network) and the $GABA_AR$ reversal
497 potential was that of P10 (J4 network). We find that the resulting neuronal activity generated
498 was significantly increased compared to the control P20 network (J1) (**Figure 9g**).
499
500 **Increased firing activity *in vivo* in the mPFC between the second and third postnatal weeks**
501 To determine whether our modeling prediction on network activity changes can be validated *in*
502 *vivo*, multisite recordings of the LFP and multi-unit activity (MUA) were performed in layers II/III
503 of mPFC at P8-10 and P20-23. A significant increase of MUA was identified at P22 compared to
504 P9 mice, indicating a developmental increased spiking activity in layers II/III of mPFC on the third
505 compared to the second postnatal week (**Figure 10**). Similarly, the spiking activity in the BC
506 augmented with age (**Supplementary Figure 7**). To characterize the firing dynamics along
507 development, we used MUA for clustering single-unit activity. We detected bursts of spikes using

508 the previously developed method (Gorin et al. 2016). The burst occurrence in the mPFC
509 increased with age (33.62±1.91 %, 161 single units at neonatal age vs. 50.12±4.91 %, 150 single
510 units at juvenile age; $p<0.0001$, One-way ANOVA, $F_{(1, 309)}=272.26$). Correspondingly, the number
511 of units organized in bursts increased with age, as well, from 21 out of 161 single units at
512 neonatal age to 104 out of 150 single units at juvenile age (**Figure 10d**). Moreover, we analyzed
513 the mPFC and BC units in their amplitude, dv/dt and half-width and detected, similarly to the in
514 vitro conditions, a significant increase in the AP amplitude and rate of rise but no difference in
515 the half-width (**Supplementary Figure 8**). These results provide further evidence that the
516 decreased excitatory synaptic activity of mPFC cannot be attributed to increased spiking activity
517 of mPFC neurons at P10.
518
519 **Discussion**
520 Our study has identified significant developmental events in the mPFC and the BC between the
521 second and third postnatal weeks. Specifically, we have shown that spontaneous inhibitory
522 transmission, measured as sIPSCs, is increased in mPFC from P10 to P20. Moreover, our data
523 support a depolarizing action of $GABA_AR$ in the second postnatal week, in the mPFC, as indicated
524 by the presence of non-AMPAR-mediated sEPSCs, depolarizing reversal potential of evoked
525 $GABA_AR$ responses, increased basal fEPSPs following $GABA_AR$ activation, which is blocked by
526 concurrent bumetanide application, and decreased protein levels of KCC2. In parallel,
527 differences the intrinsic properties of GABAergic interneurons of mice in the juvenile period
528 resemble are more mature, compared to the neonatal period in mPFC. The above
529 developmental adaptations, along with increased AP amplitude and AP rate-of-rise in pyramidal
530 cells age result in augmented network activity in the juvenile mPFC, compared to the neonatal
531 mPFC.
532
533 **Depolarizing action of GABA in the immature cortex**
534 GABA plays a crucial role in inhibiting adult neurons, acting primarily via the chloride-permeable
535 $GABA_AR$ and resulting in hyperpolarization of the membrane potential (Kaila and Voipio 1987).
536 However, GABA action leads to depolarization of immature neurons (i.e. during the first
537 postnatal week in mice), due to an initially higher intracellular chloride concentration $[Cl^-]_{in}$ (Ben-
538 Ari 2001; Ben-Ari et al. 2007; Ben-Ari 2012). The developmental switch of GABA action from
539 depolarizing to hyperpolarizing results from changes in cation-chloride co-transporter

540 expression: NKCC1, a cation-Cl^- importer, is highly expressed in neuronal precursor cells during
541 early brain development (Plotkin et al. 1997; Yamada et al. 2004), while the expression of the
542 K^+-Cl^- cotransporter 2 (KCC2), a cation-Cl^- exporter, increases after the first postnatal week (Ben-
543 Ari 2001; Ben-Ari et al. 2007; Ben-Ari 2012). This increased KCC2 transporter expression might
544 provide a central mechanism for the depolarization to hyperpolarization switch of GABAergic
545 transmission via progressive reduction of $[Cl^-]_{in}$ (Lu et al. 1999; Rivera et al. 1999; Ganguly et al.
546 2001; Ben-Ari 2002; Dzhala et al. 2005; Fiumelli et al. 2005).
547 The $GABA_AR$ switch from depolarizing to hyperpolarizing occurs at P7 in the hippocampus,
548 cortex, amygdala (Ben-Ari et al. 1989; Luhmann and Prince 1991; LoTurco et al. 1995; Owens et
549 al. 1996; Martina et al. 2001; Gulledge and Stuart 2003; Ben-Ari et al. 2007). The most
550 developmentally delayed switch in the GABAergic polarity has identified in the mPFC. In Rinetti-
551 Viargas et al., 2017, they showed that the $GABA_A$ signaling matures around birth at dendrites
552 and after preadolescent period (~P20) at axon initial segment of prefrontal pyramidal neuros.
553 They showed the changes in local chloride transporters function using gramicidin-based
554 perforated patch recordings and applied GABA via an iontophoretic pipette. We reinforce the
555 $GABA_A$ signaling change using evoked IPSC recordings in the soma if prefrontal pyramidal
556 neurons.
557 Our study suggests that this switch is delayed in the mPFC compared to primary somatosensory
558 cortex and it takes place between P10 and P20. Specifically, we show that increased $GABA_AR$
559 activity leads to enhanced fEPSPs in neonatal mPFC (P10), suggesting that the $GABA_AR$ function
560 is depolarizing in the mPFC at P10. This enhancement is prevented in the presence of the NKCC1
561 blocker, bumetanide. Furthermore, diazepam increases the number of spontaneous activity
562 events in the brain slice, which is also prevented in the presence of bumetanide. This hypothesis
563 is further supported by decreased levels of KCC2 transporter in the neonatal mPFC and it is
564 conceded the age- dependent differences in membrane NKCC1 and KCC2 protein level and
565 phosphorylation (Rinetti-Viargas et al., 2017) Our results could have implications for
566 understanding the protracted maturation of mPFC compared to other cortical areas, which may
567 depend on a combination of a delayed switch from depolarizing-to-hyperpolarizing function of
568 $GABA_AR$ and maturation of interneurons.
569
570 **Interneurons and mPFC development**

571 Recordings of Lhx6^{+}- interneurons indicate that both passive and active properties are regulated
572 by age and reach values that better resemble adult MGE-derived interneurons. Specifically, we
573 have found that the input resistance and AP width decrease while the AP rate of rise increases
574 in the mPFC at P20 compared to P10. In part, similar findings have been identified for PV^{+} cells
575 in the hippocampus (Doischer et al. 2008; Miyamae et al. 2017) and SST^{+} cells in the anterior
576 cingulate cortex (Pan et al. 2017). On the other hand, the AHP amplitude is still quite immature
577 in the mPFC at P20, compared to PV^{+}, SST^{+} interneurons in primary sensory areas or the
578 hippocampus and compared to adult mPFC (Doischer et al. 2008; Yang et al. 2013; Pan et al.
579 2017). Therefore, it is likely that the physiological properties of PV+ and SST+ interneurons in
580 the mPFC continue to change past the third postnatal week.
581 Our knowledge on the neonatal physiology of mPFC GABAergic interneurons is very limited. It
582 has been shown that PV expression is lowest in juveniles and increases during adolescence to
583 levels similar to those observed in adulthood (Caballero et al. 2014). Furthermore, PV expression
584 is not evident in the neonatal period and emerges during the juvenile period in the mPFC (del
585 Rio et al. 1994; de Lecea et al. 1995; Zheng et al. 2011; Spampanato and Sullivan 2016). Our
586 results agree with these findings, as PV expression was detected in very low amounts during the
587 juvenile period in the mPFC.
588 In addition, our study has identified decreased excitatory and increased inhibitory synaptic
589 function between the second and third postnatal weeks. We show that the frequency of sIPSCs
590 in layer II/III pyramidal cells of mPFC increases from neonatal to juvenile period, consistent with
591 the developmental changes of IPSCs in layer III pyramidal neurons of monkey PFC (González-
592 Burgos et al. 2015) and mouse mPFC (Kroon et al. 2019).
593
594 **Pyramidal neurons and network activity**
595 It has been suggested that spontaneous network activity changes from local, highly synchronized
596 to more diffuse from the second to the third postnatal weeks, in the primary sensory cortices
597 (Golshani et al. 2009; Frye and MacLean 2016). Oscillatory activity in the mPFC first emerges at
598 P15 (Bitzenhofer et al. 2019). In this study, we have found increased spiking activity in the mPFC
599 during the third, compared to the second postnatal week. This occurred despite the decreased
600 excitatory and increased inhibitory synaptic function, but could be explained partly by the
601 developmental increase of AP amplitude and rate of rise in the mPFC layer II/III pyramidal

602 neurons, which could be due to the on-going maturation of sodium channels in pyramidal
603 neurons.
604 Studies in developing mPFC pyramidal neurons have proposed that there is a unique sensitive
605 time window for synaptic maturation of these neurons from individual cortical layers. During rat
606 mPFC layer V development, the intrinsic properties, synaptic inputs and morphology of
607 pyramidal neurons develop together during early postnatal life. While the greatest changes were
608 reported during the first ten days after birth, the adult-like properties emerged after the end of
609 the third week (P21) (Zhang et al. 2011). This study confirms that the second postnatal week is
610 a period of rapid growth, similar to that in other neocortical regions by combining functional and
611 structural measurements of developing pyramidal neurons in mouse mPFC (Zhu 2000; Romand
612 et al. 2011).
613 **Developmental PFC malformation leads to cognitive disorders in adulthood**
614 The neonatal functional maturation of GABAergic circuits and E/I (excitation to inhibition)
615 balance are critical for PFC-dependent behaviours and plasticity in the adult while their
616 malfunction leads to many psychiatric disorders (Benes 1991; Kilb 2012; Ferguson and Gao
617 2018). From the prenatal period to late adolescence, the PFC network is highly vulnerable to
618 genetic and environmental factors (Andersen 2003), since the mPFC is one of the latest cortical
619 regions to develop (Huttenlocher 1990). While many studies have focused on understanding
620 several developmental processes during adolescence (Caballero et al. 2016), our knowledge
621 regarding the ongoing cellular and network developmental processes during the perinatal period
622 is notably limited, despite significant evidence showing that environmental manipulations
623 during this period manifest as complex psychiatric and neurologic disorders in adulthood
624 (Weinberger 1986).
625 The delayed developmental shift of GABA action in various mouse models mimicking human
626 brain disorders have been investigated, including the maternal immune activation model
627 (Corradini et al. 2018; Fernandez et al. 2018), the Scn1a and Scn1b mouse models of Dravet
628 syndrome (Yuan et al., 2019), the 22q11.2 deletion syndrome (Amin et al. 2017) and the Fmr1
629 deficient model of fragile X syndrome (He et al. 2018). In the latter study, early postnatal
630 correction of GABA depolarization (bumetanide-treated) led to sufficient normalization of the
631 mature BC network (He et al. 2018). The impaired KCC2 has been proposed as a potential
632 therapeutic target of epilepsies by many studies in animal models and human patients (Moore
633 et al. 2017).

634 Our study focuses in understanding the early developmental cellular and physiological
635 mechanisms of mPFC circuits, before adolescence, and proposes that the neonatal mPFC
636 compared to BC exhibits a delayed switch from depolarization to hyperpolarization function of
637 $GABA_AR$. Our results raise the possibility that the delayed maturation of mPFC compared to other
638 cortical areas depends on a combination of a delayed switch from depolarization to
639 hyperpolarization function of the $GABA_AR$ and delayed maturation of interneurons.
640

641 **Acknowledgements:**

642 Authors are grateful to Emmanuella Foinikianaki for her help with Matlab analysis and histology
643 and to Giasemi Eptaminitaki for her help in *in situ* hybridization experiments. They also would
644 like to thank all the members of Karagogeos and Sidiropoulou Labs and the animal facility of the
645 IMBB for help with experiments. This study was co-financed through the Operational Program
646 "Education and Lifelong Learning" of the National Strategic Reference Framework – Research
647 Funding Program (EDBM34) by a grant to DK (10040) and through the BIOIMAGING-GR, National
648 Roadmap for Research Infrastructures from the European Union (European Social Fund-ESF) and
649 Greek National Funds. KK has been a recipient of the Manasaki fellowship and a Medical School
650 fellowship of the University of Crete and a poster award at the 27th Hellenic Society for
651 Neuroscience Meeting.

652 **Author Contributions:**

653 All experiments were conceived and designed by K.K., K.S., and D.K. All experiments performed
654 by K.K., A.V., O.C. and X.X. Computational simulations were performed by K.S. Data
655 were analyzed by K.K., A.V., O.C., M.D. K.S. and discussed with D.K. X.X. and I.L.H.-O. X.X. carried
656 out and analyzed the *in vivo* experiments. Manuscript was written by K.K., D.K. and K.S. All
657 authors discussed and commented on the manuscript.

658

659 **References:**

660 Allene C, Cattani A, Ackman JB, Bonifazi P, Aniksztejn L, Ben-Ari Y, Cossart R. 2008. Sequential
661 Generation of Two Distinct Synapse-Driven Network Patterns in Developing Neocortex. J
662 Neurosci. 28:12851–12863.
663 Amin H, Marinaro F, De Pietri Tonelli D, Berdondini L. 2017. Developmental excitatory-to-
664 inhibitory GABA-polarity switch is disrupted in 22q11.2 deletion syndrome: a potential
665 target for clinical therapeutics. Scientific Reports. 1–18.
666 Andersen SL. 2003. Trajectories of brain development: point of vulnerability or window of
667 opportunity? Neuroscience & Biobehavioral Reviews. 27:3–18.
668 Bahrey HLP, Moody WJ. 2003. Early Development of Voltage-Gated Ion Currents and Firing
669 Properties in Neurons of the Mouse Cerebral Cortex. Journal of Neurophysiology. 89:1761–
670 1773.
671 Bartolini G, Ciceri G, Marin O. 2013. Integration of GABAergic Interneurons into Cortical Cell
672 Assemblies: Lessons from Embryos and Adults. 79:849–864.
673 Ben-Ari Y. 2001. Developing networks play a similar melody. Trends in Neurosciences. 24:353–
674 360.
675 Ben-Ari Y. 2002. Excitatory actions of gaba during development: the nature of the nurture. Nat
676 Rev Neurosci. 3:728–739.
677 Ben-Ari Y. 2012. Refuting the challenges of the developmental shift of polarity of GABA actions:
678 GABA more exciting than ever! 1–18.
679 Ben-Ari Y, Cherubini E, Corradetti R, Gaiarsa JL. 1989. Giant synaptic potentials in immature rat
680 CA3 hippocampal neurones. The Journal of Physiology. 416:303–325.
681 Ben-Ari Y, Gaiarsa JL, Tyzio R, Khazipov R. 2007. GABA: A Pioneer Transmitter That Excites
682 Immature Neurons and Generates Primitive Oscillations. Physiological Reviews. 87:1215–
683 1284.
684 Ben-Ari Y, Khalilov I, Kahle KT, Cherubini E. 2012. The GABA Excitatory/Inhibitory Shift in Brain
685 Maturation and Neurological Disorders. The Neuroscientist. 18:467–486.
686 Bendotti C, Hohmann C, Forloni G, Brain RRD, 1990. 1990. Developmental expression of
687 somatostatin in mouse brain. II. In situ hybridization. Elsevier. 53:26–39.
688 Benes FM. 1991. Deficits in Small Interneurons in Prefrontal and Cingulate Cortices of
689 Schizophrenic and Schizoaffective Patients. Archives of General Psychiatry. 48:996–1001.
690 Best JR, Miller PH. 2010. A Developmental Perspective on Executive Function. Child
691 Development. 81:1641–1660.

692 Bitzenhofer SH, Ahlbeck J, Wolff A, Wiegert JS, Gee CE, Oertner TG, Hanganu-Opatz IL. 2017.
693 Layer-specific optogenetic activation of pyramidal neurons causes beta-gamma entrainment
694 of neonatal networks. Nature Communications. 8:14563.
695 Bitzenhofer SH, Poepplau JA, Chini M, Marquardt A, Hanganu-Opatz I. 2019. Activity-dependent
696 maturation of prefrontal gamma oscillations sculpts cognitive performance. bioRxiv. 1–39.
697 Bitzenhofer SH, Sieben K, Siebert KD, Spehr M, Hanganu-Opatz IL. 2015. Oscillatory Activity in
698 Developing Prefrontal Networks Results from Theta-Gamma-Modulated Synaptic Inputs.
699 CellReports. 11:486–497.
700 Brockmann MD, Pöschel B, Cichon N, Hanganu-Opatz IL. 2011. Coupled Oscillations Mediate
701 Directed Interactions between Prefrontal Cortex and Hippocampus of the Neonatal Rat.
702 Neuron. 71:332–347.
703 Burgard EC, Hablitz JJ. 1993. Developmental changes in NMDA and non-NMDA receptor-
704 mediated synaptic potentials in rat neocortex. Journal of Neurophysiology. 69:230–240.
705 Caballero A, Flores-Barrera E, Cass DK, Tseng KY. 2014. Differential regulation of parvalbumin
706 and calretinin interneurons in the prefrontal cortex during adolescence. Brain Struct Funct.
707 219:395–406.
708 Caballero A, Granberg R, Tseng KY. 2016. Mechanisms contributing to prefrontal cortex
709 maturation during adolescence. Neuroscience & Biobehavioral Reviews. 1–29.
710 Casey BJ, Giedd JN, Thomas KM. 2000. Structural and functional brain development and its
711 relation to cognitive development. Biological Psychology. 54:241–257.
712 Chalkiadaki K, Velli A, Kyriazidis E, Stavroulaki V, Vouvoutsis V, Chatzaki E, Aivaliotis M,
713 Sidiropoulou K. 2019. Development of the MAM model of schizophrenia in mice: Sex
714 similarities and differences of hippocampal and prefrontal cortical function.
715 Neuropharmacology 144, 193–207.
716 Chini, M. & Hanganu-Opatz, I. L. 2020. Prefrontal Cortex Development in Health and Disease:
717 Lessons from Rodents and Humans. *Trends Neurosci*
718 Clancy B, Darlington RB, Neuroscience BF, 2001. 2001. Translating developmental time across
719 mammalian species. Elsevier. 105:7–17.
720 Corradini I, Focchi E, Rasile M, Morini R, Desiato G, Tomasoni R, Lizier M, Ghirardini E, Fesce R,
721 Morone D, Barajon I, Antonucci F, Pozzi D, Matteoli M. 2018. Maternal Immune Activation
722 Delays Excitatory-to-Inhibitory Gamma-Aminobutyric Acid Switch in Offspring. Biological
723 Psychiatry. 83:680–691.

724 de Lecea L, del Ri o JA, Soriano E. 1995. Developmental expression of parvalbumin mRNA in the
725 cerebral cortex and hippocampus of the rat. Molecular Brain Research. 32:1–13.
726 DeFelipe J, Fariñas I. 1992. The pyramidal neuron of the cerebral cortex: Morphological and
727 chemical characteristics of the synaptic inputs. Progress in Neurobiology. 39:563–607.
728 del Rio J, De Lecea L, Ferrer I, Soriano E. 1994. The development of parvalbumin-
729 immunoreactivity in the neocortex of the mouse. 81:247–259.
730 Del Rio JA, Soriano E, Ferrer I. 1992. Development of GABA-immunoreactivity in the neocortex
731 of the mouse. J Comp Neurol. 326:501–526.
732 Diamond A. 2005. Normal Development of Prefrontal Cortex from Birth to Young Adulthood:
733 Cognitive Functions, Anatomy, and Biochemistry. In: Principles of Frontal Lobe Function.
734 Oxford University Press. p. 466–503.
735 Doischer D, Aurel Hosp J, Yanagawa Y, Obata K, Jonas P, Vida I, Bartos M. 2008. Postnatal
736 Differentiation of Basket Cells from Slow to Fast Signaling Devices. J Neurosci. 28:12956–
737 12968.
738 Dzhala VI, Talos DM, Sdrulla DA, Brumback AC, Mathews GC, Benke TA, Delpire E, Jensen FE,
739 Staley KJ. 2005. NKCC1 transporter facilitates seizures in the developing brain. Nature
740 Medicine 2005 11:11. 11:1205–1213.
741 Ferguson BR, Gao W-J. 2018. PV Interneurons: Critical Regulators of E/I Balance for Prefrontal
742 Cortex-Dependent Behavior and Psychiatric Disorders. Front Neural Circuits. 12:479–13.
743 Fernandez A, Dumon C, Guimond D, Tyzio R, Bonifazi P, Lozovaya N, Burnashev N, Ferrari DC,
744 Ben-Ari Y. 2018. The GABA Developmental Shift Is Abolished by Maternal Immune Activation
745 Already at Birth. Cerebral Cortex. 130:e1447–11.
746 Fiumelli H, Cancedda L, Poo M-M. 2005. Modulation of GABAergic Transmission by Activity via
747 Postsynaptic Ca2+-Dependent Regulation of KCC2 Function. Neuron. 48:773–786.
748 Forloni G, Hohmann C, Research JCDB, 1990. 1990. Developmental expression of somatostatin
749 in mouse brain. I. Immunocytochemical studies. Elsevier. 53:6–25.
750 Frye CG, MacLean JN. 2016. Spontaneous activations follow a common developmental course
751 across primary sensory areas in mouse neocortex. Journal of Neurophysiology. 116:431–
752 437.
753 Fuster J. 2015. The Prefrontal Cortex. Academic Press.
754 Ganguly K, Schinder AF, Wong ST, Poo M-M. 2001. GABA Itself Promotes the Developmental
755 Switch of Neuronal GABAergic Responses from Excitation to Inhibition. Cell. 105:521–532.

Golshani P, Goncalves JT, Khoshkhoo S, Mostany R, Smirnakis S, Portera-Cailliau C. 2009. Internally Mediated Developmental Desynchronization of Neocortical Network Activity. J Neurosci. 29:10890–10899.

Gorin, M., C. Tsitoura, A. Kahan, K. Watznauer, D. R. Drose, M. Arts, R. Mathar, S. O'Connor, I. L. Hanganu-Opatz, Y. Ben-Shaul and M. Spehr (2016). "Interdependent Conductances Drive Infraslow Intrinsic Rhythmogenesis in a Subset of Accessory Olfactory Bulb Projection Neurons." The Journal of Neuroscience 36(11): 3127-3144.

González-Burgos G, Miyamae T, Pafundo DE, Yoshino H, Rotaru DC, Hoftman G, Datta D, Zhang Y, Hammond M, Sampson AR, Fish KN, Bard Ermentrout G, Lewis DA. 2015. Functional Maturation of GABA Synapses During Postnatal Development of the Monkey Dorsolateral Prefrontal Cortex. Cerebral Cortex. 25:4076–4093.

Gulledge AT, Stuart GJ. 2003. Excitatory Actions of GABA in the Cortex. Neuron. 37:299–309.

Guo ZV, Li N, Huber D, Ophir E, Gutnisky D, Ting JT, Feng G, Svoboda K. 2014. Flow of Cortical Activity Underlying a Tactile Decision in Mice. Neuron. 81:179–194.

He Q, Arroyo ED, Smukowski SN, Xu J, Piochon C, Savas JN, Portera-Cailliau C, Contractor A. 2018. Critical period inhibition of NKCC1 rectifies synapse plasticity in the somatosensory cortex and restores adult tactile response maps in fragile X mice. Mol Psychiatry. 8:109–116.

Heidbreder CA, Groenewegen HJ. 2003. The medial prefrontal cortex in the rat: evidence for a dorso-ventral distinction based upon functional and anatomical characteristics. Neuroscience & Biobehavioral Reviews. 27:555–579.

Hensch TK. 2016. The Power of the Infant Brain. Nature Publishing Group. 314:64–69.

Huguenard JR, Hamill OP, Prince DA. 1988. Developmental changes in Na+ conductances in rat neocortical neurons: appearance of a slowly inactivating component. Journal of Neurophysiology. 59:778–795.

Huttenlocher PR. 1990. Morphometric study of human cerebral cortex development. Neuropsychologia. 28:517–527.

Kaila K, Voipio J. 1987. Postsynaptic fall in intracellular p H induced by GABA-activated bicarbonate conductance. Nature. 330:163–165.

Khazipov R, Luhmann HJ. 2006. Early patterns of electrical activity in the developing cerebral cortex of humans and rodents. Trends in Neurosciences. 29:414–418.

Khazipov R, Minlebaev M, Valeeva G. 2013. Early gamma oscillations. Neuroscience. 250:240–252.

788 Khazipov R, Sirota A, Leinekugel X, Holmes GL, Ben-Ari Y, Buzsáki G. 2004. Early motor activity
789 drives spindle bursts in the developing somatosensory cortex. Nature. 432:758–761.
790 Kilb W. 2012. Development of the GABAergic System from Birth to Adolescence. The
791 Neuroscientist. 18:613–630.
792 Kirmse K, Kummer M, Kovalchuk Y, Witte OW, Garaschuk O, Holthoff K. 2015. GABA depolarizes
793 immature neurons and inhibits network activity in the neonatal neocortex in vivo. Nature
794 Communications. 6:7750.
795 Kolb B, Mychasiuk R, Muhammad A, Li Y, Frost DO, Gibb R. 2012. Experience and the developing
796 prefrontal cortex. Proc Natl Acad Sci USA. 109:17186–17193.
797 Konstantoudaki X, Papoutsi A, Chalkiadaki K, Poirazi P, Sidiropoulou K. Modulatory effects of
798 inhibition on persistent activity in a cortical microcircuit model. Front Neural Circuits. 2014
799 Jan 31;8:7.
800 Konstantoudaki X, Chalkiadaki K, Tivodar S, Karagogeos D, Sidiropoulou K. 2016. Impaired
801 synaptic plasticity in the prefrontal cortex of mice with developmentally decreased number
802 of interneurons. Neuroscience. 1–13.
803 Kriegstein AR, Suppes T, Prince DA. 1987. Cellular and synaptic physiology and epileptogenesis
804 of developing rat neocortical neurons in vitro. Developmental Brain Research. 34:161–171.
805 Kroeze Y, Oti M, van Beusekom E, Cooijmans RHM, van Bokhoven H, Kolk SM, Homberg JR, Zhou
806 H. 2017. Transcriptome Analysis Identifies Multifaceted Regulatory Mechanisms Dictating a
807 Genetic Switch from Neuronal Network Establishment to Maintenance During Postnatal
808 Prefrontal Cortex Development. Cerebral Cortex. 1–19.
809 Kroon T, van Hugte E, van Linge L, Mansvelder HD, Meredith RM. 2019. Early postnatal
810 development of pyramidal neurons across layers of the mouse medial prefrontal cortex.
811 Scientific Reports. 9:5037–16.
812 Le Magueresse C, Monyer H. 2013. GABAergic Interneurons Shape the Functional Maturation of
813 the Cortex. Neuron. 77:388–405.
814 Liodis P, Denaxa M, Grigoriou M, Akufo-Addo C, Yanagawa Y, Pachnis V. 2007. Lhx6 Activity Is
815 Required for the Normal Migration and Specification of Cortical Interneuron Subtypes.
816 Journal of Neuroscience. 27:3078–3089.
817 LoTurco JJ, Owens DF, Heath MJS, Davis MBE, Kriegstein AR. 1995. GABA and glutamate
818 depolarize cortical progenitor cells and inhibit DNA synthesis. Neuron. 15:1287–1298.

819 Lu J, Karadsheh M, Delpire E. 1999. Developmental regulation of the neuronal-specific isoform
820 of K-CL cotransporter KCC2 in postnatal rat brains. J Neurobiol. 39:558–568.
821 Luhmann HJ, Prince DA. 1991. Postnatal maturation of the GABAergic system in rat neocortex.
822 Journal of Neurophysiology. 65:247–263.
823 Martina M, Royer S, Paré D. 2001. Cell-Type-Specific GABA Responses and Chloride Homeostasis
824 in the Cortex and Amygdala. Journal of Neurophysiology. 86:2887–2895.
825 McCormick DA, Prince DA. 1987. Post-natal development of electrophysiological properties of
826 rat cerebral cortical pyramidal neurones. The Journal of Physiology. 393:743–762.
827 Miyamae T, Chen K, Lewis DA, González-Burgos G. 2017. Distinct physiological maturation of
828 parvalbumin-positive neuron subtypes in mouse prefrontal cortex. J Neurosci. 3325–16–48.
829 Moore YE, Kelley MR, Brandon NJ, Deeb TZ, Moss SJ. 2017. Seizing Control of KCC2: A New
830 Therapeutic Target for Epilepsy. Trends in Neurosciences. 40:555–571.
831 Mòdol L, Bollmann Y, Tressard T, Baude A, Che A, Duan ZRS, Babij R, De Marco García NV, Cossart
832 R. 2019. Assemblies of Perisomatic GABAergic Neurons in the Developing Barrel Cortex.
833 Neuron. 1–18.
834 Owens DF, Boyce LH, Davis MBE, Kriegstein AR. 1996. Excitatory GABA Responses in Embryonic
835 and Neonatal Cortical Slices Demonstrated by Gramicidin Perforated-Patch Recordings and
836 Calcium Imaging. J Neurosci. 16:6414–6423.
837 Pan G, Yang J-M, Hu X-Y, Li X-M. 2017. Postnatal development of the electrophysiological
838 properties of somatostatin interneurons in the anterior cingulate cortex of mice. Nature
839 Publishing Group. 1–12.
840 Plotkin MD, Snyder EY, Hebert SC, Delpire E. 1997. Expression of the Na-K-2Cl cotransporter is
841 developmentally regulated in postnatal rat brains: A possible mechanism underlying GABA's
842 excitatory role in immature brain. J Neurobiol. 33:781–795.
843 Ramoa AS, McCormick DA. 1994. Developmental changes in electrophysiological properties of
844 LGNd neurons during reorganization of retinogeniculate connections. J Neurosci. 14:2089–
845 2097.
846 Rinetti-Vargas, Gina, Khanhky Phamluong, Dorit Ron, and Kevin J. Bender. 2017. “Periadolescent
847 Maturation of GABAergic Hyperpolarization at the Axon Initial Segment.” *CellReports*
848 20(1):21–29.

849 Rivera C, Voipio J, Payne JA, Ruusuvuori E, Lahtinen H, Lamsa K, Pirvola U, Saarma M, Kaila K.
850 1999. The K+/Cl- co-transporter KCC2 renders GABA hyperpolarizing during neuronal
851 maturation. Nature. 397:251–255.
852 Romand S, Wang Y, Toledo-Rodriguez M, Markram H. 2011. Morphological Development of
853 Thick-Tufted Layer V Pyramidal Cells in the Rat Somatosensory Cortex. Front Neuroanat. 5.
854 Rossant C, Kadir SN, Goodman DFM, et al. Spike sorting for large, dense electrode arrays. *Nat*
855 *Neurosci*. 2016;19(4):634-641. doi:10.1038/nn.4268
856 Schaeren-Wiemers N, Gerfin-Moser A. 1993. A single protocol to detect transcripts of various
857 types and expression levels in neural tissue and cultured cells: in situ hybridization using
858 digoxigenin-labelled cRNA probes. Histochemistry. 100:431–440.
859 Schubert D, Martens GJM, Kolk SM. 2014. Molecular underpinnings of prefrontal cortex
860 development in rodents provide insights into the etiology of neurodevelopmental disorders.
861 20:795–809.
862 Southwell DG, Paredes MF, Galvao RP, Jones DL, Froemke RC, Sebe JY, Alfaro-Cervello C, Tang Y,
863 García-Verdugo JM, Rubenstein JL, Baraban SC, Alvarez-Buylla A. 2012. Intrinsically
864 determined cell death of developing cortical interneurons. Nature. 491:109–113.
865 Spampanato J, Sullivan R. 2016. Development and physiology of GABAergic feedback excitation
866 in parvalbumin expressing interneurons of the mouse basolateral amygdala. Physiological
867 …. 4:e12664–15.
868 Tsujimoto S. 2008. The prefrontal cortex: functional neural development during early childhood.
869 The Neuroscientist. 14:345–358.
870 Van De Werd HJJM, Rajkowska G, Evers P, Uylings HBM. 2010. Cytoarchitectonic and
871 chemoarchitectonic characterization of the prefrontal cortical areas in the mouse. Brain
872 Struct Funct. 214:339–353.
873 Weinberger DR. 1986. Physiologic Dysfunction of Dorsolateral Prefrontal Cortex in
874 Schizophrenia. Archives of General Psychiatry. 43:114.
875 Yamada J, Okabe A, Toyoda H, Kilb W, Luhmann HJ, Fukuda A. 2004. Cl− uptake promoting
876 depolarizing GABA actions in immature rat neocortical neurones is mediated by NKCC1. The
877 Journal of Physiology. 557:829–841.
878 Yang JM, Zhang J, Yu YQ, Duan S, Li XM. 2013. Postnatal Development of 2 Microcircuits Involving
879 Fast-Spiking Interneurons in the Mouse Prefrontal Cortex. Cerebral Cortex. 24:98–109.

880 Yuan Y, Malley HAOX, Smaldino MA, Bouza AA, Hull JM, Isom LL. 2019. Delayed maturation of
881 GABAergic signaling in the Scn1a and Scn1b mouse models of Dravet Syndrome. Scientific
882 Reports. 1–16.
883 Zhang Z, Jiao Y-Y, Sun Q-Q. 2011. Developmental maturation of excitation and inhibition balance
884 in principal neurons across four layers of somatosensory cortex. Neuroscience. 174:10–25.
885 Zheng K, An JJ, Yang F, Xu W. 2011. TrkB signaling in parvalbumin-positive interneurons is critical
886 for gamma-band network synchronization in hippocampus. Proc Natl Acad Sci USA; 108
887 (41):17201-17206;
888 Zhu JJ. 2000. Maturation of layer 5 neocortical pyramidal neurons: amplifying salient layer 1 and
889 layer 4 inputs by Ca2+ action potentials in adult rat tuft dendrites. The Journal of Physiology.
890 526:571–587.
891 **Figures and figure legends**
892
893

Figure 1

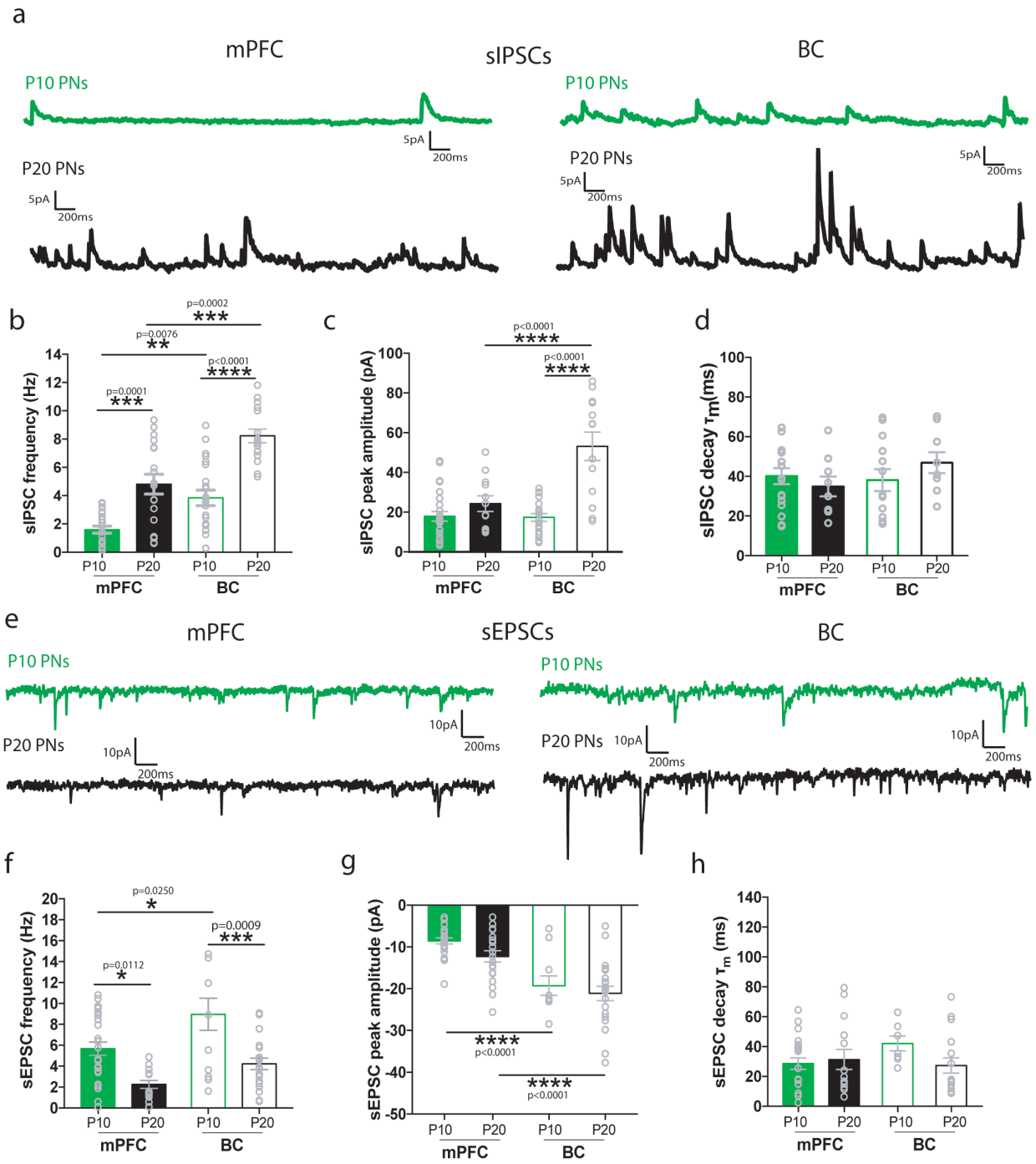

Figure 1. Properties of sIPSCs and sEPSCs at P10 and P20 of layer II/III mPFC and BC pyramidal neurons

(a) Representative traces of spontaneous inhibitory postsynaptic currents (sIPSCs) from layer II/III mPFC (left) and BC (right) pyramidal neurons at P10 (green) and P20 (black).

(b) Bar graph showing the sIPSC frequency (Hz) at P10 and P20 mPFC and BC pyramidal neurons. Two-way ANOVA analyses showed a significant effect of age ($F_{(1,26)}$=19.286, p<0.001) and brain

901 area ($F_{(1,26)}$=12.554, p=0.002) and a trend towards significance of age*brain interaction
902 ($F_{(1,26)}$=3.826, p=0.063).
903 **(c)** Bar graph showing the sIPSC peak amplitude at P10 and P20 of mPFC and BC pyramidal
904 neurons. Two-way ANOVA analyses showed a trend towards significance in the brain area factor
905 ($F_{(1,26)}$=3.420, p=0.077) and no effect of age ($F_{(1,26)}$=1.981 p=0.177) or area*age interaction
906 ($F_{(1,26)}$=0.050, p=0.826).
907 **(d)** Bar graph showing the sIPSC decay time constant (τm) at P10 to P20 of mPFC and BC
908 pyramidal neurons. Two-way ANOVA analyses did not show any significant effect of age
909 ($F_{(1,26)}$=1.129, p=0.299), brain area ($F_{(1, 26)}$=0.211, p=0.651) or area*age interaction ($F_{(1, 26)}$=1.052,
910 p=0.316) was found.
911 **(e)** Representative traces of spontaneous excitatory postsynaptic currents (sEPSCs) from layer
912 II/III mPFC (left) and BC (right) pyramidal neurons at P10 (green) and P20 (black).
913 **(f)** Bar graph showing the sEPSC frequency at P10 to P20 of mPFC and BC pyramidal neurons.
914 Two-way ANOVA analyses showed a significant effect of age ($F_{(1,25)}$=5.273, p=0.032) and brain
915 area ($F_{(1,25)}$=7.388, p=0.013), but not a significant interaction age*brain area ($F_{(1,25)}$=0.591,
916 p=0.450)
917 **(g)** Bar graph showing the sEPSCs peak amplitude at P10 to P20 of mPFC and BC pyramidal
918 neurons. Two-way ANOVA analyses did not reveal significant effect of brain area ($F_{(1,25)}$=0.853,
919 p=0.366), age ($F_{(1,25)}$=0.144, p=0.708) or interaction ($F_{(1,25)}$=0.712, p=0.408).
920 **(h)** Bar graph showing the sEPSCs decay time constant (τm) at P10 to P20 of mPFC and BC
921 pyramidal neurons. Two-way ANOVA analyses showed no significant effect of age ($F_{(1,25)}$=0.557,
922 p=0.463), brain area ($F_{(1,25)}$=0.720, p=0.405) or interaction ($F_{(1,25)}$=1.128, p=0.300).
923 *n=9-13 cells from 5-9 mice/age group.
924

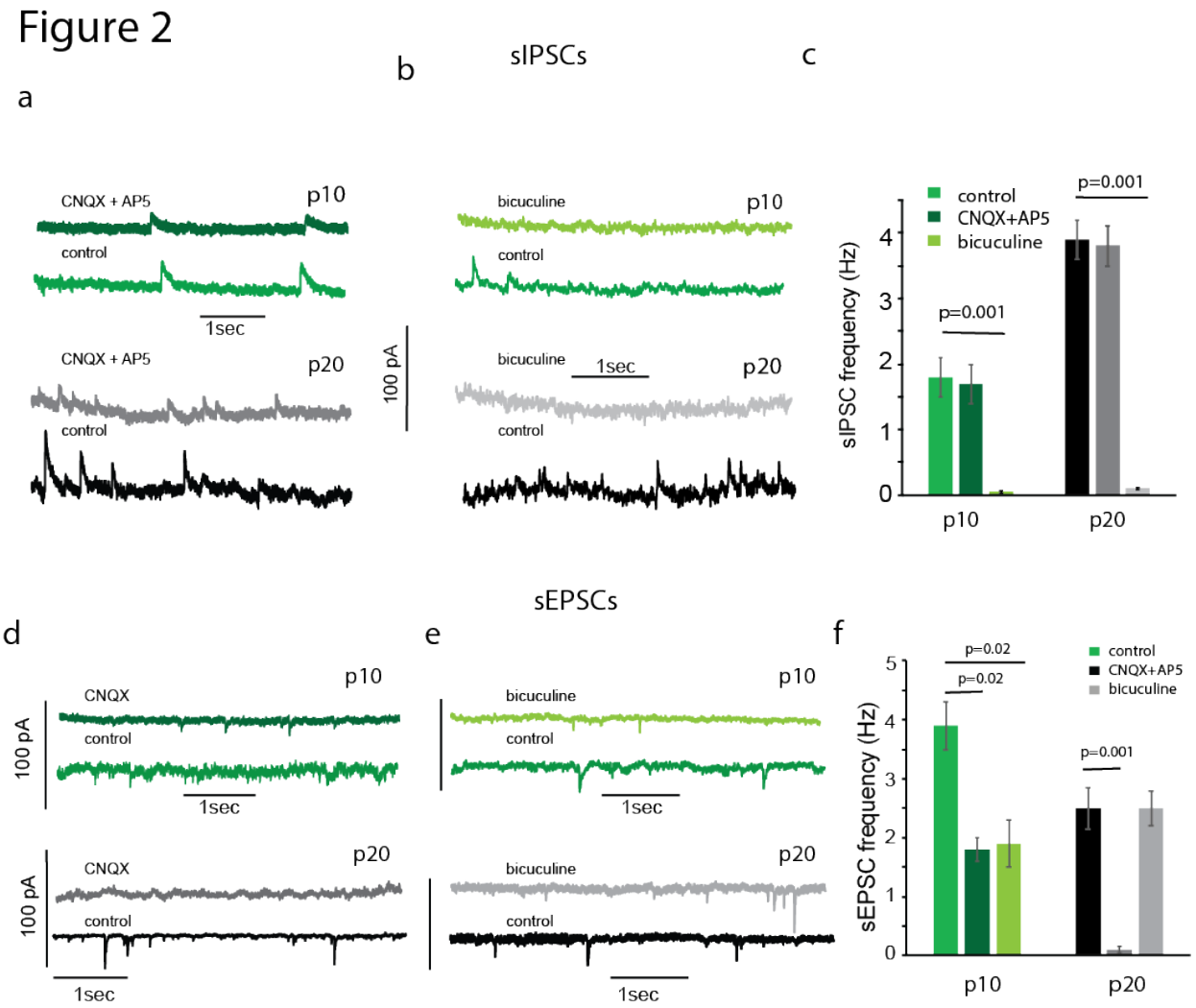

Figure 2- sIPSCs and sEPSCs frequency at P10 and P20 of layer II/III mPFC and BC pyramidal neurons

Text not aligned

(a) Representative traces showing that CNQX+AP5 did not alter the sIPSC frequency either at P10 or P20 mPFC (recorded at +10mV).

(b) Representative traces showing that bicuculine blocks sIPSCs either at P10 or P20 mPFC (recorded at +10mV).

(c) Graphs showing that bicuculine blocks the sIPSCs in P10 and P20 mPFC (t-test, p=0.001), while CNQX+AP5 does not have an effect (t-test, p=0.5).

(d) Representative traces showing that CNQX reduces sEPSC frequency at p10 and blocks sEPSCs at P20 mPFC (recorded at -70mV).

(e) Representative traces showing that bicuculine reduces sEPSC frequency at p10 and does not affect sEPSCs at P20 mPFC (recorded at -70mV).

939 **(f)** Graphs showing that at P10 mPFC both CNQX+AP5 and bicuculine reduces the sEPSC
940 frequency in P10 mPFC (t-test, p=0.03 for both drugs), while in P20 mPFC only CNQX+AP5 blocks
941 sEPSCs.
942
943
944
945
946
947
948
949
950
951
952
953
954
955
956
957
958
959
960
961
962
963
964
965

Figure 3

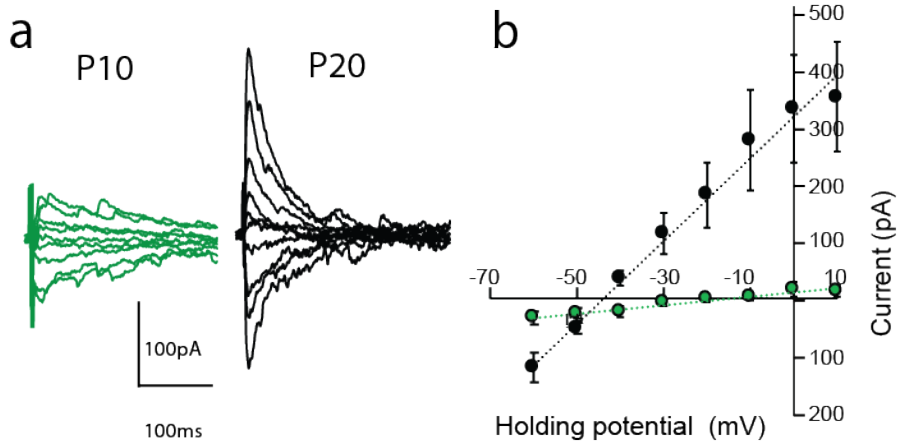

Figure 3 – The reversal potential for evoked IPSCs is depolarized at p10 mPFC compared to p20

(a) Representative traces of evoked IPSCs at p10 and p20 mPFC

(b) Graph showing the average of eIPSCs at different holding potentials.

Figure 4

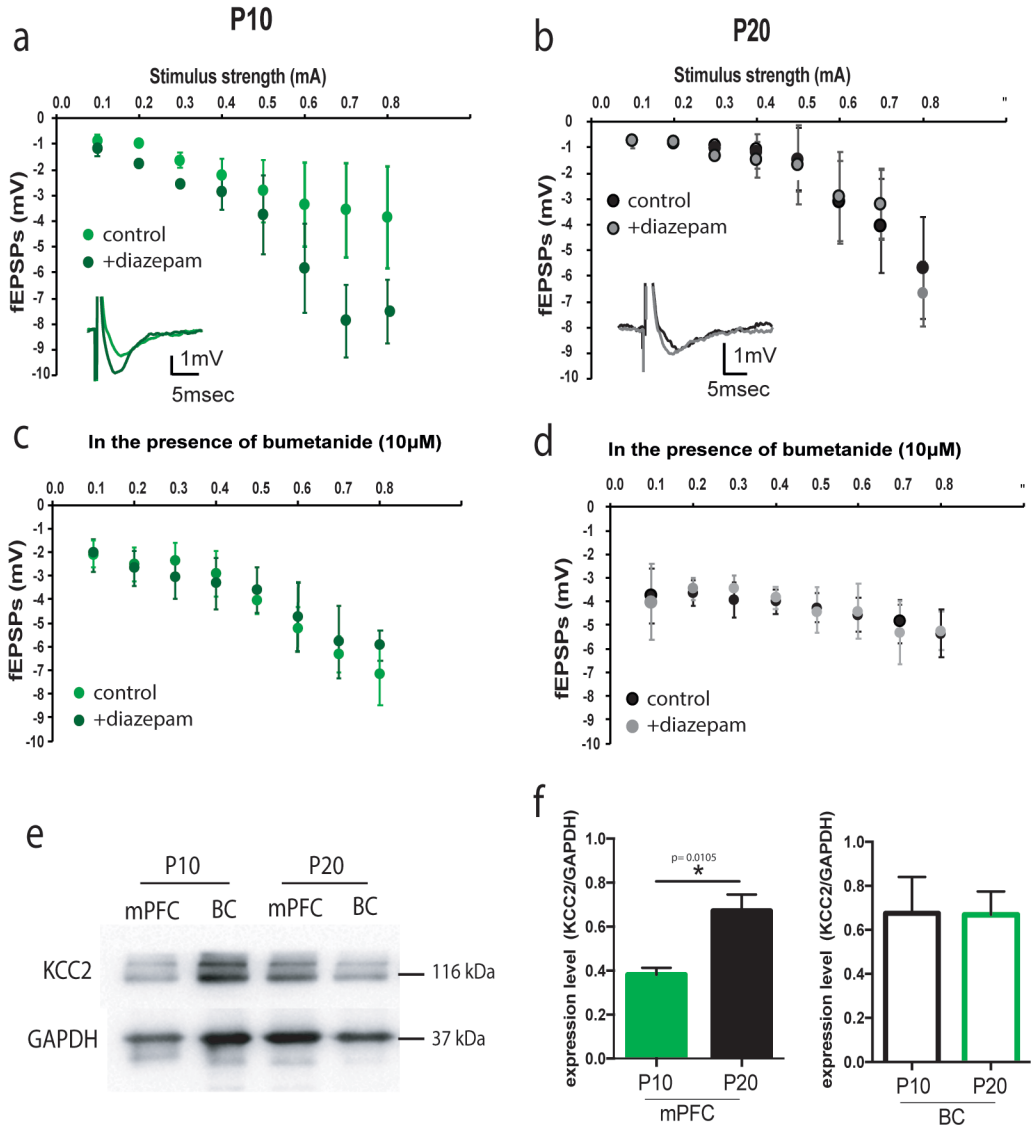

Figure 4. Changes in the chloride transporters mediate the depolarizing action of $GABA_AR$ at p10 mPFC

fEPSPs were recorded were recorded in layer II/III mPFC in response to current pulses of increasing stimulus strength of layer II/III, during two experimental treatments, before and after application of 2μM diazepam ($GABA_AR$ agonist) at P10 and P20.

(a) Representative traces (left) and graph (right) showing the fEPSPs amplitude before (green) and after (dark green) diazepam bath application (in the presence of CNQX and AP5), in mPFC at P10. Two-way repeated measures ANOVA analyses of evoked fEPSPs revealed significant effect of stimulus strength ($F_{(1,7)} = 20.64$, $p=0.004$) and experimental treatments ($F_{(1,7)} = 5.025$, $p=0.036$) (n=2 brain slices from 3-4 mice).

983 **(b)** Graph (right) and representative traces (left) showing that diazepam bath application does
984 not have any effect on the fEPSP amplitude in mPFC at P20 (in the presence of CNQX and AP5).
985 Two-way repeated measures ANOVA analyses of evoked fEPSPs revealed a significant effect of
986 stimulus strength ($F_{(1,7)}$ = 10.36, $p<0.0001$) but not experimental treatment ($F_{(1,7)}$=0.03,
987 p=0.9382), (n=2 brain slices from 3-4 mice).
988 **(c)** Graph showing that the effect of diazepam on fEPSP is occluded in the presence of
989 bumetanide (plus CNQX and AP5) at P10. Two-way repeated measures ANOVA analyses of
990 evoked fEPSPs did not reveal a significant effect of experimental treatment ($F_{(1,7)}$=0.08, p=0.752),
991 (n=2 brain slices from 3-4 mice).
992 **(d)** Graph showing the effect of diazepam on fEPSP in the presence of bumetanide (plus CNQX
993 and AP5) at P20. Two-way repeated measures ANOVA analyses of evoked fEPSPs did not reveal
994 a significant effect of experimental treatment ($F_{(1,7)}$=0.06, p=0.831), (n=2 brain slices from 3-4
995 mice).
996 **(e)** Representative blots showing changes of the K-Cl co-transporter (KCC2) levels, relative to
997 GAPDH at P10 and P20 in mPFC and BC.
998 (f) Graph showing the normalized protein level (KCC2/GAPDH) in mPFC at P10 and P20. The KCC2
999 protein levels was significantly increased at P20 compared to P10 in mPFC (two-tailed t-test, p=
1000 0.01) but not in BC (two-tailed t-test, p= 0.97) (n=3-4 mice).
1001
1002
1003
1004
1005
1006
1007
1008
1009
1010
1011
1012
1013
1014

Figure 5

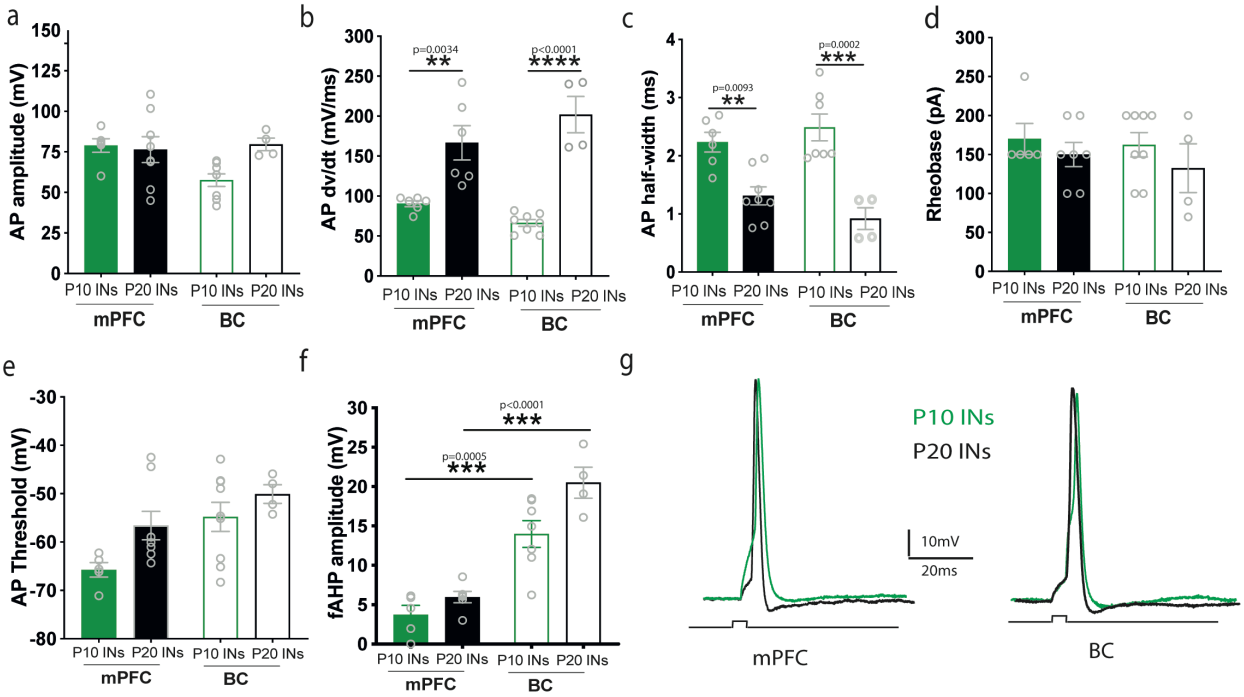

Figure 5. Poor development of active membrane properties of Lhx6⁺ interneurons in mPFC.

(a) Bar graph showing the action potential (AP) amplitude of interneurons at P10 and P20 in mPFC and BC. Two-way ANOVA analyses did not show any significant effect of age ($F_{(1,22)}$=2.46, p=0.13) or brain area ($F_{(1, 22)}$=2.13, p=0.15) was found., (n=6-9 cells from 5-6 mice/age group).

(b) Bar graph showing the AP rate of rise (dv/dt) of interneurons at P10 and P20 in mPFC and at P10 in BC. Two-way ANOVA analyses showed a significant effect between ages ($F_{(1,20)}$=58.96, p<0.0001) but not brain area ($F_{(1,20)}$=0.16 p=0.69). Post-hoc analysis showed that the AP rate of rise significantly increased at P20 compared to P10 in mPFC (Tukey's test, p=0.0034) and at P20 compared to P10 in BC (Tukey's test, p<0.001), (n=6-9 cells from 5-6 mice/age group).

(c) Bar graph showing the AP duration (half-width) of interneurons at P10 and P20 in mPFC and BC. Two-way ANOVA analyses showed a significant effect between ages ($F_{(1,21)}$=39.16, p<0.0001) but not brain area ($F_{(1,21)}$=0.16 p=0.73). Post-hoc analysis showed that the AP duration significantly decreased at P20 compared to P10 in mPFC (Tukey's test, p= 0.0093) and at P20 compared to P10 in BC (Tukey's test, p=0.0002), (n=6-9 cells from 5-6 mice/age group).

(d) Bar graph showing the AP rheobase of interneurons at P10 and P20 in mPFC and BC. Two-way ANOVA analyses did not show any significant effect of age ($F_{(1,20)}$=1.60, p=0.22) or brain area ($F_{(1, 20)}$=0.40, p=0.53) was found.

1034 **(e)** Bar graph showing the AP threshold of interneurons at P10 and P20 in mPFC and BC. . Two-
1035 way ANOVA analyses showed significant effect of age ($F_{(1,22)}$=5.048, p=0.035) and brain area ($F_{(1,}$
1036 $_{22)}$=8.00, p=0.009) was found. Post-hoc analysis showed that the AP threshold was not
1037 significantly different at P20 compared to P10 in mPFC (Tukey's test, p=0.1673) and in BC
1038 (Tukey's test, p=0.72009) or at P10 in mPFC compared to P10 in BC (Tukey's test, p=0.067) and
1039 at P20 in mPFC compared to P20 in BC (Tukey's test, p=0.72).
1040 **(f)** Bar graph showing the AHP (afterhypolarization) amplitude of interneurons at P10 and P20
1041 in mPFC and BC. Two-way ANOVA analyses showed significant effect of age ($F_{(1,18)}$=7.35,
1042 p=0.0143) and brain area ($F_{(1, 18)}$=63.72, p<0.0001) was found. Post-hoc analysis showed that the
1043 AHP amplitude was not significantly different at P20 compared to P10 in mPFC (Tukey's test,
1044 p=0.7187) and was significantly decreased in mPFC compered to BC, at P10 (Tukey's test, p=
1045 0.0005) and in mPFC compered to BC at P20 (Tukey's test, p<0.00001), (n=6-9 cells from 5-6
1046 mice/age group).
1047 **(g)** Bar graph showing the AHP time of interneurons at P10 and P20 in mPFC and BC. Two-way
1048 ANOVA analyses did not show any significant effect of age ($F_{(1,19)}$=0.009, p=0.92) or brain area
1049 ($F_{(1, 19)}$=1.074, p=0.31) was found.
1050 **(h)** Representative traces of APs of layer II/III Lhx6+ interneurons in mPFC (left) and BC (right)
1051 at P10 (green) and P20 (black).
1052

Figure 6

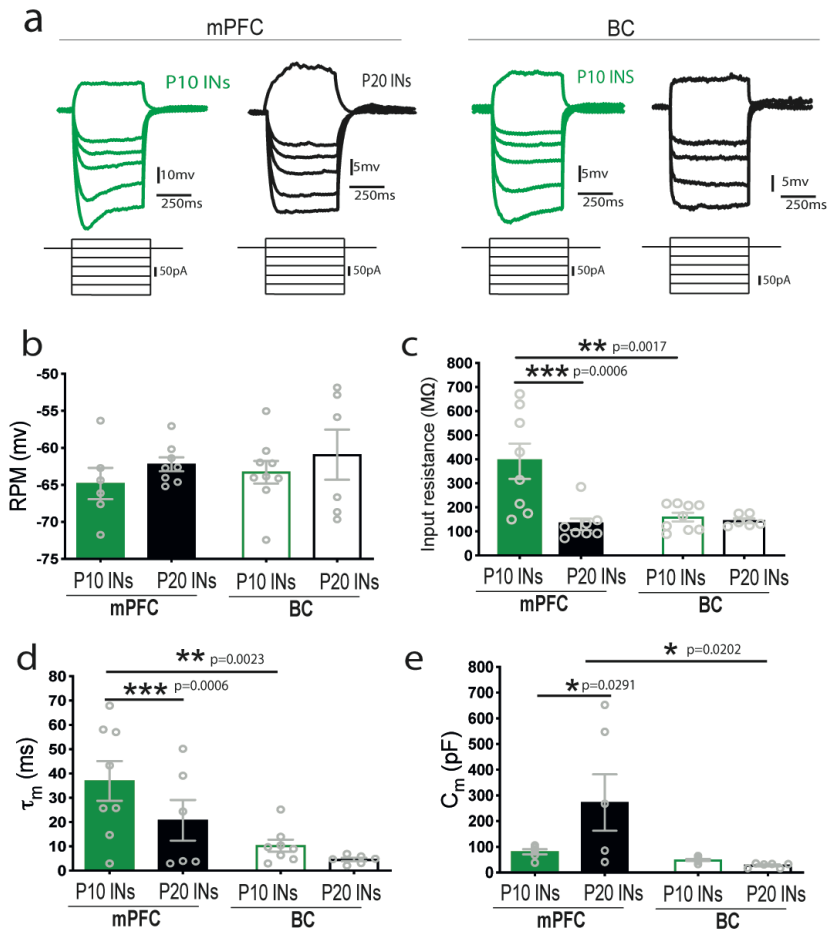

Figure 6. Passive membrane properties of Lhx6+ interneurons at P10 and P20 mPFC and P10 BC.

(a) Representative voltage responses (top traces) to 500ms positive and negative current pulses (bottom traces, +50, -50, -70, -100, -150, -200 pA) in mPFC at P10 and P20 and BC of Lhx6+ florescent interneurons from layer II/III.

(b) Bar graph showing the resting membrane potential (RMP) of interneurons at P10 and P20 in mPFC and BC. Two-way ANOVA analyses did not show any significant effect of age ($F_{(1,25)}$=1.55, p=0.22) or brain area ($F_{(1, 25)}$=0.50, p=0.48) was found., (n=6-9 cells from 5-6 mice/age group).

(c) Bar graph showing the input resistance of interneurons at P10 and P20 in mPFC and BC. Two-way ANOVA analyses showed a significant effect of age ($F_{(1,27)}$=10.94, p=0.0027) and brain area ($F_{(1,27)}$=6.65 p=0.0157). Post-hoc analysis showed that the input resistance significantly decreased at P20 compared to P10 in mPFC (Tukey's test, p=0.0006) and was significantly higher in mPFC compared with BC, at P10 (Tukey's test, p=0.0017), (n=8-9 cells from 5-6 mice/age group).

1068 **(d)** Bar graph showing the membrane time constant (τ_m) of interneurons at P10 and P20 in
1069 mPFC and BC. Two-way ANOVA analyses showed a significant effect of age ($F_{(1,24)}$=14.71,
1070 p=0.0008) and brain area ($F_{(1,24)}$=6.92 p=0.0147). Post-hoc analysis showed that τ_m was
1071 significantly higher at P10 compared to P20 in mPFC (Tukey's test, p=0.0006) while it was
1072 significantly higher in mPFC compared to BC, at P10 (Tukey's test, p=0.0023), (n=8-9 cells from
1073 5-6 mice/age group).
1074 **(e)** Bar graph showing the membrane capacitance (C_m) of interneurons at P10 and P20 in mPFC
1075 and BC. Two-way ANOVA analyses showed a significant effect between brain areas ($F_{(1,21)}$=6.82,
1076 p=0.00163) and not between ages ($F_{(1,21)}$=2.60 p=0.1219). Post-hoc analysis showed that Cm was
1077 significantly higher at P10 compared with P20 in mPFC (Tukey's test, p=0.0291) and was not
1078 significantly different between mPFC and BC, at P10 (Tukey test, p=0.97) while it was significantly
1079 higher at P20 in mPFC compared to P20 in BC (Tukey test, p=0.0202), (n=6-9 cells from 5-6
1080 mice/age group).
1081
1082
1083
1084
1085

Figure 7

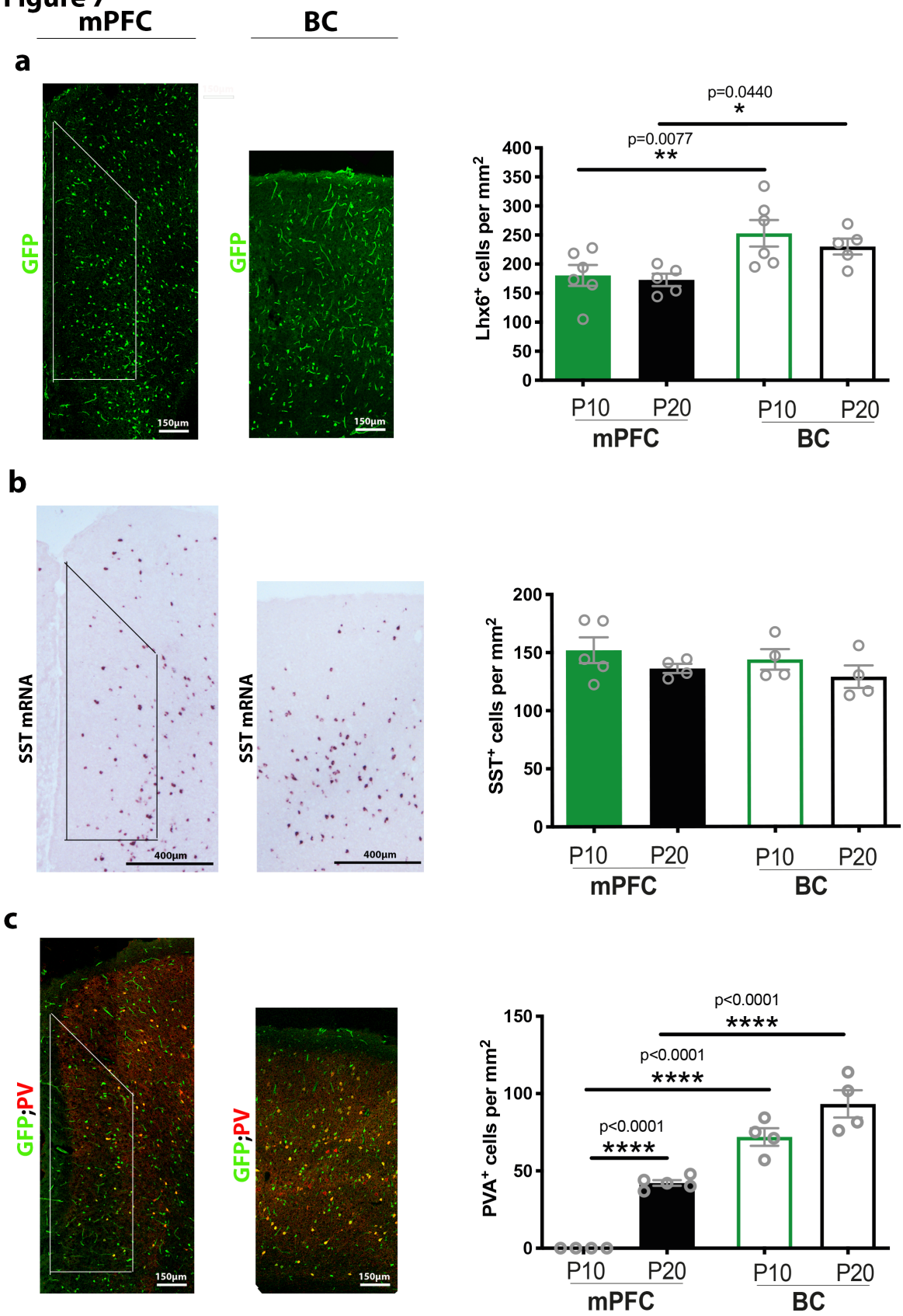

1086

1087 **Figure 7. Significant differences in cellular density of Lhx6$^+$ interneurons in mPFC and BC at P10**
1088 **and P20.**
1089 **(a)** A representative immunostaining with GFP for Lhx6$^+$ interneurons in Lhx6-cre;ROSA26fl-
1090 STOPfl-YFP mice in mPFC and BC at P20 is showing on the left. Scale bars: 150 µm. On the right,
1091 bar graph comparing Lhx6$^+$ interneurons cell density (per mm^2) at P10 and P20 in mPFC and BC.
1092 Two-way ANOVA analyses of the cell density revealed a significant effect of brain area ($F_{(1, 18)}$) =
1093 13.11, p=0.0020), but not of age ($F_{(1,18)}$=0.7185, p=0.4078). Post-hoc analysis showed that the
1094 Lhx6$^+$ cell density was not significant different at P20 compared to P10 in mPFC and BC (LSD test,
1095 p=0.77 and p= 0.38, respectively). The Lhx6$^+$ cell density was significantly lower in mPFC
1096 compared to BC at P10 and P20, respectively (LSD test, p=0.0077 and p= 0.0440, respectively),
1097 (P10 in mPFC and BC:n= 5 mice, P20 in mPFC and BC: n=4).
1098 **(b)** A representative in situ hybridization staining for somatostatin positive cells (SST$^+$) using
1099 wild type animals in mPFC and BC at P20 is showing on the left. Scale bar: 200µm. Bar graph
1100 comparing cell density based on SST$^+$ expression at P10 and P20 in mPFC and BC. Two-way
1101 ANOVA analyses of the cell density showed no significant effect of age ($F_{(1, 13)}$= 2.78, p=0.12) and
1102 brain area ($F_{(1,13)}$=071, p=0.41) was found, (P10 in mPFC: n= 5 mice, P10 in BC and P20 in mPFC
1103 and BC: n=4).
1104 **(c)** A representative double immunostaining for GFP; PV (PV: parvalbumin) in mPFC and BC at
1105 P20 is showing on the left. Scale bars: 150 µm. On the right, bar graph comparing cell density
1106 based on PV$^+$ expression at P10 and P20 in mPFC and BC. Two-way ANOVA analyses of the cell
1107 density revealed a significant effect of age ($F_{(1, 14)}$ = 45.49, p<0.0001) and brain area ($F_{(1, 14)}$ =
1108 170.2, p<0.0001). PV$^+$ cells were not found in mPFC but were identified in BC, at P10. Post-hoc
1109 analysis showed that the PV$^+$ cell density was not significantly different at P20 compared to P10
1110 in BC (LSD test, p= 0.1089), but was significantly lower in mPFC compared to BC at P20 (LSD test,
1111 p<0.0001), (P10 and P20 in mPFC: n= 5 mice, P10 and P20 in BC: n=4).
1112
1113
1114
1115
1116
1117
1118

Figure 8

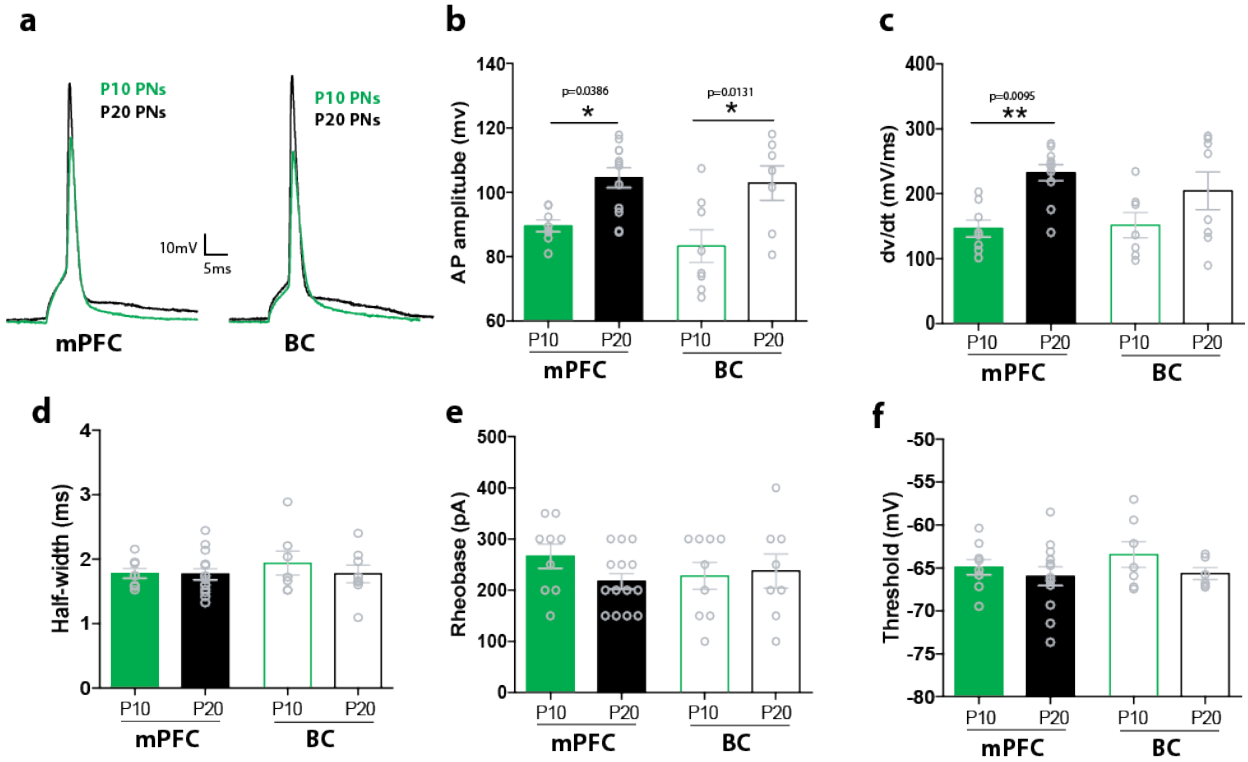

Figure 8. Active properties of mPFC and BC pyramidal neurons.

(a) Representative traces of action potentials (APs) of layer II/III pyramidal neurons in mPFC (left) and BC (right) at P10 (green) and P20 (black), respectively.

(b) Bar graph showing the AP amplitude of pyramidal neurons at P10 and P20 in mPFC and BC. Two-way ANOVA analyses showed a significant effect of age ($F_{(1, 31)} = 18.74$, p=0.0001) but not on brain area ($F_{(1, 31)} = 0.99$, p=0.32) was found. Post-hoc analysis showed that the AP amplitude significantly increased at P20 compared to P10 in mPFC and BC (Tukey's test, p=0.0386 and p= 0.0131, respectively) (n=9-14 cells from 6-10 mice/age group).

(c) Bar graph showing the AP rate of rise (dv/dt) of pyramidal neuron at P10 and P20 in mPFC and BC. Two-way ANOVA analyses showed a significant effect of age ($F_{(1,30)}= 13.53$, p=0.0009) but not on brain area ($F_{(1, 30)} = 0.36$, p=0.55) was found. Post-hoc analysis showed that the AP rate of rise significantly increased at P20 compared to P10 in mPFC (Tukey's test, p= 0.0095), but not in BC (Tukey's test, p= 0.25) (n=8-14 cells from 6-10 mice/age group).

1135 **(d)** Bar graph showing the AP duration (half-width) of pyramidal neuron at P10 and P20 in mPFC
1136 and BC. Two-way ANOVA analyses showed no significant effect of age ($F(1, 33) = 0.52$, $p=0.47$)
1137 or brain area ($F_{(1, 33)} = 0.43$, $p=0.51$) was found (n=9-14 cells from 6-10 mice/age group).
1138 **(e)** Bar graph showing the AP rheobase of pyramidal neuron at P10 and P20 in mPFC and BC.
1139 Two-way ANOVA analyses showed no significant effect of age ($F_{(1, 36)} = 0.66$, $p=0.41$) or brain
1140 area ($F_{(1, 36)} = 0.16$, $p=0.69$) was found (n=9-14 cells from 6-10 mice/age group).
1141 **(f)** Bar graph showing the AP threshold of pyramidal neuron at P10 and P20 in mPFC and BC.
1142 Two-way ANOVA analyses showed no significant effect of age ($F_{(1,31)} = 1.90$, $p=0.17$) or brain area
1143 ($F_{(1,31)}=0.55$, $p=0.46$) was found (n=9-14 cells from 6-10 mice/age group).
1144
1145

Figure 9

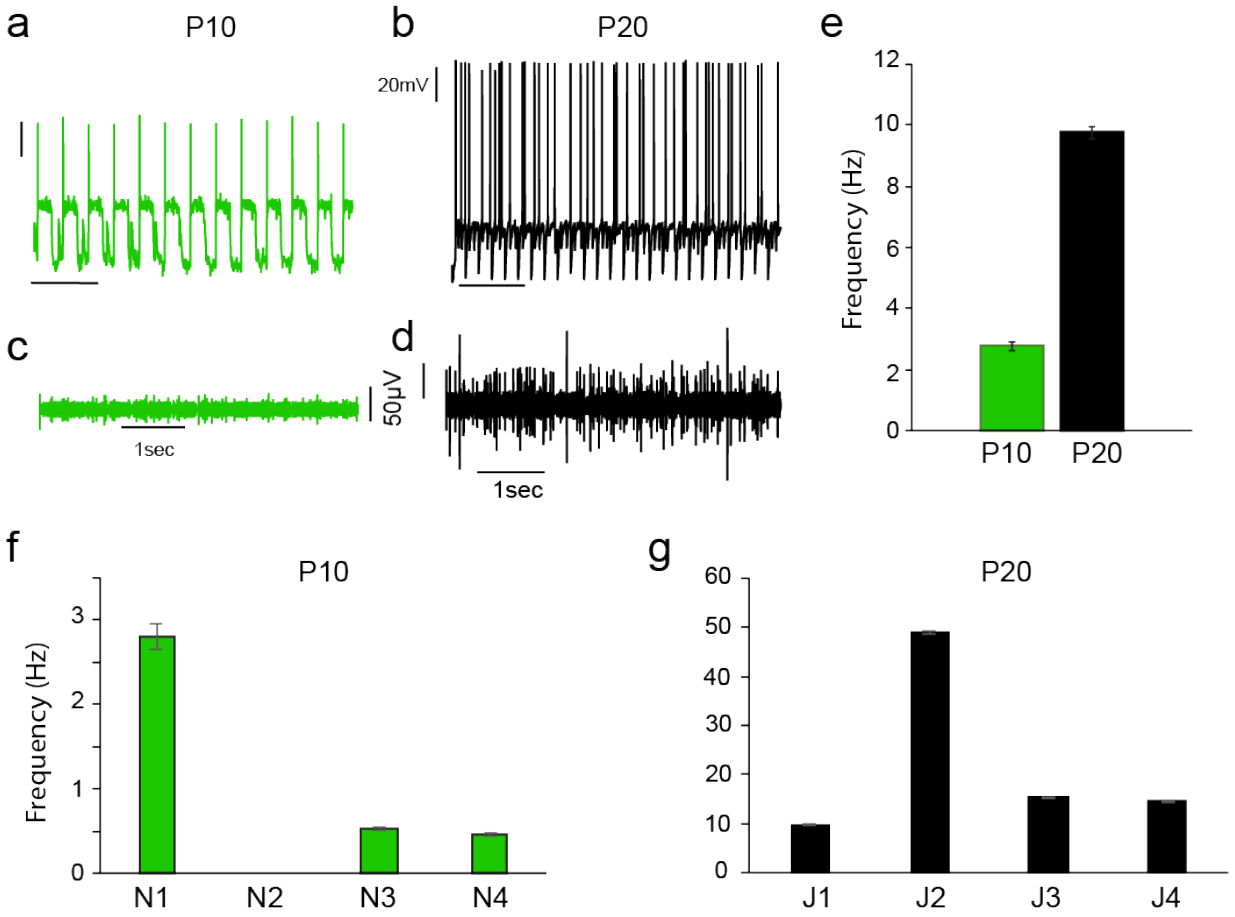

Figure 9. Modeling p10 and p20 PFC network activity

(a,b) Neuronal response of a single neuron within the PFC model network at p10 and p20

(c, d) The filtered voltage response of the p10 and p20 model networks

(e) Average frequency of the P10 and P20 model networks.

(f) Graph showing how the responses change in modified P10 model networks. N1: control P10 model network, N2: pyramidal model neuron of P20 model network used, N3: fast-spiking interneuron model network of P20 model network used, N4: GABAAR reversal potential was set to -60mV (that of P20 model network).

(g) Graph showing how the responses change in modified P20 model networks. J1: control P20 model network, J2: pyramidal model neuron of P10 model network used, J3: fast-spiking

interneuron model network of P10 model network used, J4: GABAAR reversal potential was set to -40mV (that of P10 model network).

Figure 10

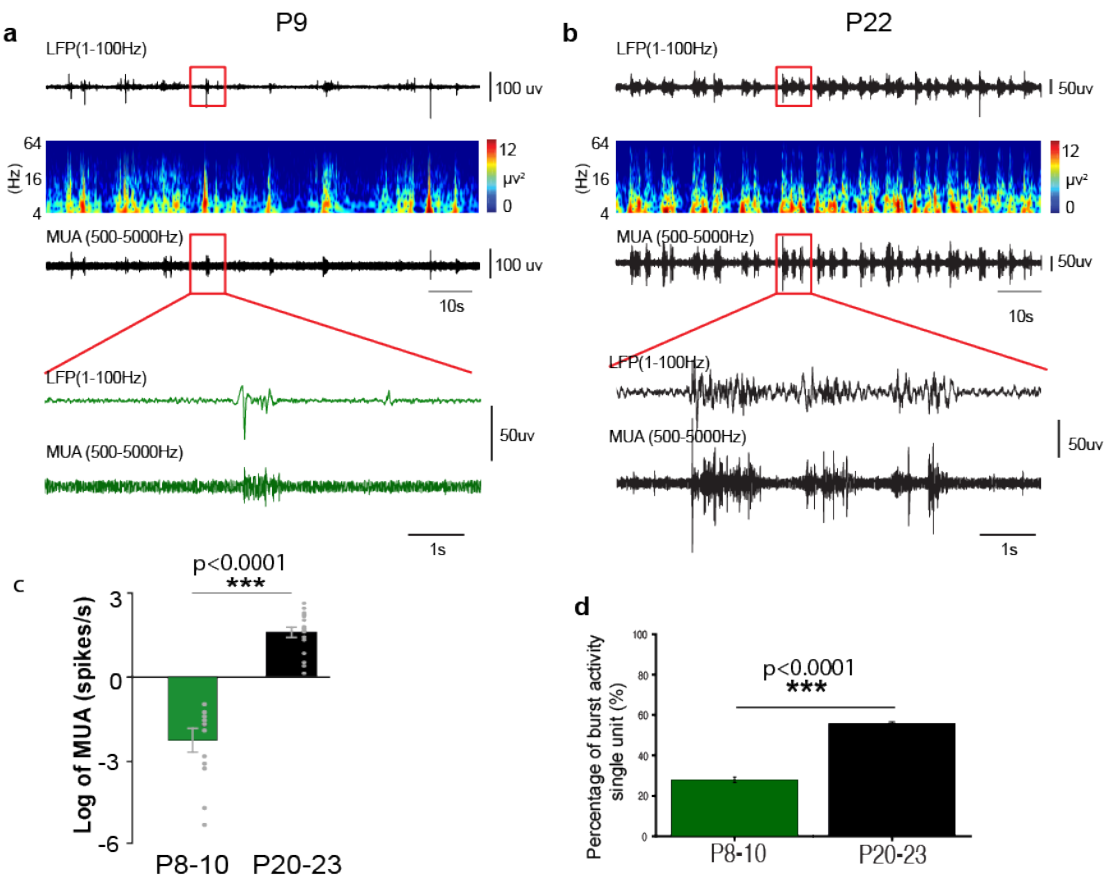

Figure 10. Spike activity in PFC of neonatal and juvenile mice.

(a) Extracellular LFP recordings of oscillatory activity in PFC from a P9 mouse displayed after bandpass (1-100 Hz) filtering (top) and the corresponding MUA after bandpass (500-5000 Hz) filtering (bottom). Traces are accompanied by the color-coded wavelet spectra of the LFP at identical time scale.

(b) the same display as (**a**), but in one P22 mouse.

(c) Bar diagram displaying the mean MUA of neurons in PFC of neonatal and juvenile mice. During development, significant increase of MUA in PFC in juvenile mice (n=14) compared with in neonatal mice (n=13) (1.71±0.16 vs. -2.29±0.45, $p<0.0001$, One-way ANOVA, $F_{(1, 25)}=80.19$).

(d) Bar diagram displaying the percentage of the burst activity of single units in PFC of neonatal and juvenile mice. During development, significant more burst activity per single unit in PFC in juvenile mice (150 single unit) than in neonatal mice (161 single unit) (55.73±0.92 % vs. 27.90±1.41 %, $p<0.0001$, One-way ANOVA, $F(1, 309)=272.26$). In neonatal mice, 21 out 161 single

1178 units were classified as “burst unit”. In juvenile mice, 104 out of 150 single units were classified
1179 as “burst unit”.